Published in final edited form as:
J Med Chem. 2022 December 22; 65(24): 16353–16371. doi:10.1021/acs.jmedchem.2c01174.

Potent Ruthenium−Ferrocene Bimetallic Antitumor Antiangiogenic Agent That Circumvents Platinum Resistance: From Synthesis and Mechanistic Studies to *In Vivo* Evaluation in Zebrafish

M Manikandan,
Shubhankar Gadre,
Sushanta Chhatar
Medicinal Chemistry and Cell Biology Laboratory, Department of Chemical Sciences, Tata Institute of Fundamental Research, Mumbai, Maharashtra 400005, India

Gourav Chakraborty,
Department of Developmental Biology, Agharkar Research Institute, Pune, Maharashtra 411004, India

Naushad Ahmed,
Department of Chemistry, Indian Institute of Technology Hyderabad, Sangareddy, Telangana 502085, India

Chinmoy Patra,
Malay Patra

Abstract

Emergence of resistance in cancer cells and dose-limiting side effects severely limit the widespread use of platinum (Pt) anticancer drugs. Multi-action hybrid anticancer agents that are constructed by merging two or more pharmacophores offer the prospect of circumventing issues of Pt drugs. Herein, we report the design, synthesis, and in-depth biological evaluation of a ruthenium−ferrocene (Ru-Fc) bimetallic agent [(η^6-*p*-cymene)Ru(1,1,1-trifluoro-4-oxo-4-ferrocenyl-but-2-en-2-olate)Cl] and its five analogues. Along with aquation/anation chemistry, we evaluated the *in vitro* antitumor potency, Pt cross-resistance profile, and *in vivo* antiangiogenic properties. A structure activity analysis was performed to understand the impact of Fc, CF_3, and *p*-cymene groups on the anticancer potency of the Ru-Fc hybrid. Finally, in addition to assessing cellular uptake and intracellular distribution, we demonstrated that the Ru-Fc hybrid binds to

Correspondence to: Chinmoy Patra; Malay Patra.

Corresponding Authors, Chinmoy Patra − Department of Developmental Biology, Agharkar Research Institute, Pune, Maharashtra 411004, India; cpatra@aripune.org; Malay Patra − Medicinal Chemistry and Cell Biology Laboratory, Department of Chemical Sciences, Tata Institute of Fundamental Research, Mumbai, Maharashtra 400005, India; malay.patra@tifr.res.in.

Author Contributions
M.P. designed and supervised the project. M.M., S.C., and M.P. performed cellular experiments. S.G. performed synthesis, characterization, and analytical experiments. G.C. and C.P. performed experiments on zebrafish. N.A. collected the X-ray data and solved the structure. All authors contributed to the interpretation of data and preparation of the manuscript.

Notes
The authors declare no competing financial interest.

Europe PMC Funders Author Manuscripts

nucleophilic biomolecules and produces reactive oxygen species, which causes mitochondrial dysfunction and induces ER stress, leading to poly(ADP−ribose) polymerase-mediated necroptotic cell death.

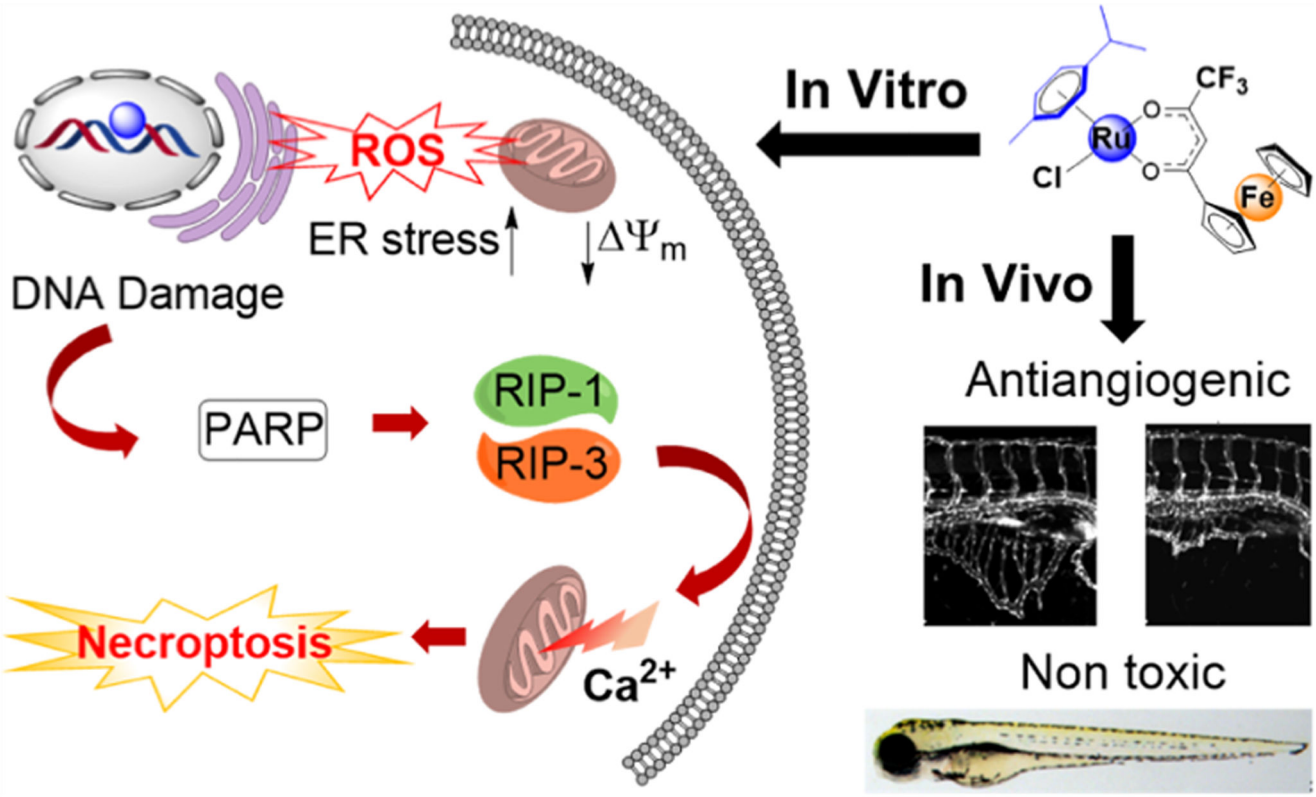

Introduction

Platinum (Pt) anticancer drugs cisplatin, carboplatin, and oxaliplatin are the frontline treatment options for a variety of localized and metastatic cancers.[1,2] These drugs enter cells either by passive diffusion or transporter-mediated uptake, undergo activation by ligand exchange, and form covalent Pt-DNA adducts, resulting in the inhibition of transcription and induction of apoptotic cancer cell death. These Pt drugs make up approximately 50% of total chemotherapeutic regimens and are therefore incorporated in the list of essential medicines by the World Health Organization (WHO).[3,4] Despite phenomenal success of platinum drugs in the clinic, a few major drawbacks such as inherent and emergence of acquired resistance in cancer cells and dose-limiting toxic side effects severely limit the actual therapeutic benefits of Pt-based chemotherapy.[1] To tackle these issues, a great deal of effort has been devoted to the development of anticancer compounds with the mechanism of action different from that of Pt drugs.[1,2,5−9]

In the recent past, growing research in the area of non-platinum anticancer agents has led to the discovery of several promising ruthenium (Ru) drug candidates as potential alternatives to Pt drugs.[7−11] The Ru(III) coordination compounds NAMI-A and KP1019,

Europe PMC Funders Author Manuscripts

developed by Allesio and Keppler, respectively, entered clinical trials, which are believed to undergo activation by a reduction in a tumor microenvironment.[7,10] Dyson's and Sadler's group developed piano-stool Ru(II)−arene organometallic complexes, such as RM175 and RAPTA-C (Figure 1), with promising antimetastatic, anti-angiogenic, and anticancer activities.[8,11] In particular, these classes of compounds exert activity through a novel mechanism of action and are capable of overcoming Pt resistance.[8,11,12]

As an alternative strategy, we and others have explored the possibility of employing multi-targeted hybrid drugs as a solution to the chemoresistance issue of Pt drugs.[2,13,14] Our recently reported bimetallic hybrids **Pt-Fc-1** and **Pt-Fc-2** (Figure 1, Fc = ferrocene) were constructed by merging two bioactive pharmacophores, namely, a DNA binder [$(NH_3)_2$Pt-(II)] or [(DACH)Pt(II)] (where DACH = 1*R*,2*R*-diaminocyclohexane) and a reactive oxygen species (ROS) inducer (ferrocenyl-β-diketonate, **L1**-H).[13] Both candidates showed excellent *in vitro* antitumor activity, and **Pt-Fc-2** exerted *in vivo* anticancer activity in an A2780 mice xenograft model.[13] We demonstrated that the Pt-Fc derivatives platinate nuclear and mitochondrial DNA, generate ROS, cause mitochondrial dysfunction, and induce severe endoplasmic reticulum (ER) stress. This multi-pronged mechanism of action of these Pt-Fc hybrids triggered non-apoptotic cell death which enables circumventing apoptosis resistance caused by down regulation of pro-apoptotic proteins Bax and Bak. We note that in contrast to apoptosis resistance which is caused by a specific mechanism (dysfunctional apoptosis signaling), Pt resistance is caused by multiple simultaneously operating mechanisms such as reduced uptake, enhanced efflux, enhanced DNA repair, and down-regulation of apoptotic proteins.[15] Comparing the potency of our cisplatin-like **Pt-Fc-1** in wild-type A2780 and its cisplatin resistant mutant A2780Cis human ovarian cancer cells revealed that the Pt-Fc hybrid has significantly lower Pt cross-resistance (resistance factor, RF = 2.8) compared to its monometallic parent drug cisplatin (RF = 9.7).[13] The purpose of this study is to design the next generation of multi-targeted hybrid anticancer agents with improved antitumor activity and, importantly, no Pt cross-resistance (expected RF ~ 1). As discussed above, encouraged by the lack of Pt cross-resistance of Ru(II)−arene compounds,[8,11,12] we envisaged substituting the [(N−N)Pt(II)] moiety in the Pt-Fc hybrids with a Ru(II)−arene moiety and constructing a bimetallic Ru-Fc hybrid **1** (Figure 1b) that is expected to have no Pt cross-resistance in cancer cells. In addition to this, the presence of the Ru(II)−arene moiety may endow **1** with antiangiogenic activity which is a key factor in tumor growth and metastasis.[16,17]

Even though synthesis and *in vitro* antitumor studies of a few Ru-Fc (**Ru1**−**Ru5**, Figure 1) derivatives were reported earlier, there is much room for improvement.[18−22] For instance, majority of these Ru-Fc derivatives showed moderate to low *in vitro* antitumor activity (discussed later). Moreover, these Ru-Fc hybrids were never evaluated for toxicity and antiangiogenic activity using any *in vivo* model. In addition to this, these previous reports did not thoroughly investigate the mechanistic aspects of Ru-Fc derivatives, such as the intracellular targets, precise mode of action, the role of individual metal centers, and the mechanism of cell death.

To this end, herein, we report the design, synthesis, and biological activity of a potent bimetallic Ru-Fc anticancer antiangiogenic agent **1** (Figure 1) and its five analogues (2−6,

Scheme 1). Along with investigating the solution stability and aquation/anation chemistry, we showed that **1** has excellent antitumor activity against a panel of cancer cell lines and has an improved Pt cross-resistance profile as compared to that of cisplatin and analogous Pt-Fc bimetallics (**Pt-Fc-1** and **Pt-Fc-2**). The potency of **1** is significantly higher as compared to that of previously reported Ru-Fc bimetallics **Ru1, Ru3**, and **Ru4** in Pt-resistant A2780Cis cells. Moreover, we analyzed the structure−activity relation (SAR) that provided insights into the impact of various functional groups on the anticancer properties of **1**. Importantly, using a zebrafish *in vivo* model we found that **1** has strong antiangiogenic properties, and it is non-toxic to zebrafish embryos at its pharmacologically effective antiangiogenic dose. Compound **1**, in particular, is the first Ru(II)−arene-containing Ru-Fc bimetallic complex identified till date which possesses both potent antitumor and antiangiogenic properties. We confirmed that while the Ru(II) center in **1** binds covalently to nucleophilic biomolecules, the Fc center catalyzes the formation of ROS from H_2O_2. Finally, in addition to assessing cellular uptake, intracellular localization, and DNA metalation, we demonstrated that **1** causes mitochondrial dysfunction and induces ER-stress through unfolded protein response (UPR), leading to poly(ADP−ribose) polymerase (PARP)-mediated necroptotic cell death.

Results and Discussion

Design, Synthesis, and Characterization of 1−6

The synthetic route to the target Ru-Fc hybrid **1** and its bimetallic (**2** and **4**) and monometallic (**3, 5**, and **6**) analogues is presented in Scheme 1. First, the β-diketone ligands 4,4,4-trifluoro-1-ferrocenylbutane-1,3-dione (**L1**),[13] 1-ferrocenylbutane-1,3-dione (**L2**),[13,23] and 1-[3-(trifluoromethyl)phenyl]-butane-1,3-dione (**L4**)[24] were synthesized by following earlier reported procedures. 4,4,4-trifluoro-1-phenylbutane-1,3-dione (**L3**) was obtained from a commercial supplier. Reaction of the $[(\eta^6\text{-arene})RuCl_2]_2$ dimer with the appropriate 1,3-diketone derivative in a MeOH/dichloromethane (DCM) mixture in the presence of NaOMe provided **1−6** in 80−90% yield.[12,25] All complexes were characterized by ^1H and ^{13}C NMR spectroscopies (Figures S1−S12) and matrix-assisted laser desorption/ionization (MALDI) mass spectrometry (Figure S13). The purity of **1−6** was confirmed to be ≥95% by elemental microanalysis (Experimental Section) and analytical high-performance liquid chromatography HPLC (Figure S14).

Our several attempts to grow X-ray-quality crystals of compounds 1−5 using a variety of solvents and methods were unsuccessful. In the case of compound **6**, the slow evaporation of methanolic solution yielded dark-red block-shaped tiny single crystals (suitable for X-ray diffraction) in a week. The X-ray structural solutions revealed that compound **6** crystallized in the monoclinic, $P2_1/c$ space group (Table S1), and its asymmetric unit (ASU) consists of a full molecule with the molecular formula $[Ru^{II}(\eta^6\text{-}C_6Me_6)(CF_3\text{-}Ar^{\text{-acac}})Cl]$ ($CF_3\text{-}Ar^{\text{-acac}}$ = **L3**-H). As shown in Figure 2, the structure of **6** confirmed the piano-stool arrangement of $\eta^6\text{-}C_6Me_6$, β-diketonate ($CF_3\text{-}Ar^{\text{-acac}}$), and Cl^- ligands around the Ru(II) center. The selected bond angle and bond distance parameters are listed in Table S2. A bond distance of 2.078 Å for the Ru−O1 bond was found to be slightly shorter than a distance of 2.091 Å for the Ru−O2 bond. This observation is not surprising as the resonating condition of $CF_3\text{-}Ar^{\text{-acac}}$ was affected by the electron-withdrawing CF_3-Ar group. The bond distance

for the Ru−Cl bond found to be 2.420 Å and the average Ru−C distance of 2.180 Å (for the η^6-C_6Me_6 bonds) are consistent with the literature report on the analogous complex [Ru(η^6-*p*-cymene) (acetylacetonate)Cl].[26] From the packing structure of **6** (Figure S15, Table S2), the closest Ru… Ru distance was found to be 7.284 Å.

Solution Stability, Aquation, and Anation Chemistry

Having complexes **1**−**6** in hand, we first studied the solution stability in water and in cell culture medium (DMEM) using **1** as a representative candidate of all six complexes. The compound is very stable in dimethylsulfoxide (DMSO) as no change was detected in the ^{1}H NMR spectrum up to 48 h (Figure S16). Then, **1** was dissolved in a mixture of DMSO-d_6/D_2O containing no NaCl or 100 mM NaCl, and ^{1}H NMR spectra were recorded at different time points. It is worth noting that 100 mM NaCl was used to mimic the extracellular physiological Cl^- concentration. As shown in Figure 3a, no significant spectral changes were observed up to 48 h in the presence of NaCl, suggesting robust aqueous stability of this class of compounds in the presence of the physiologically relevant Cl^- concentration.

However, in the absence of NaCl, addition of D_2O to a DMSO solution of **1** resulted in formation of the corresponding aqua complex as evidenced from appearance of a new singlet at 2.14 ppm (arene-CH_3, Figure 3b). The aquation was rapid, with ~95% of **1** found to be aquated within 10 min. These results are consistent with previous reports on activation of the [Ru(η^6-arene)(O−O)Cl] class of complexes through hydrolysis of the Ru−Cl bond.[12,26] Addition of 100 mM NaCl to the hydrolyzed **1** lead to rapid anation and formation of **1** in <10 min (Figure 3b), demonstrating reversible nature of the aquation and anation in the absence of and the presence of Cl^-, respectively. Then, we tested the stability of **1** in Roswell Park Memorial Institute (RPMI-1640) supplemented with 10% fetal bovine serum (FBS), a routinely used cell culture medium, using ultra-performance liquid chromatography (UPLC). Carbamazepine was used as an internal standard. As shown in Figure 3c, the peak corresponding to **1** decreased slowly with time. The decomposition was <20% upto 8 h, and approximately, 45 and 7% of **1** remained intact after 24 and 72 h, respectively, suggesting that the compound possesses good stability in cell culture media. The decomposition of **1** is most likely due to its reaction with nucleophiles such as amino acids, sugars, proteins, and so forth, present in RPMI/FBS medium.[12,27]

In Vitro Antitumor Activity, Platinum Cross-Resistance Profile, and SAR

The *in vitro* antitumor potencies of **1**−**6** were evaluated in human cervical (HeLa) and ovarian (A2780 and its cisplatin-resistant phenotype A2780Cis) cancer cells. Cells were seeded in 96-well plates and dosed with increasing concentrations of the compound, and finally, viability was measured using 3-(4,5-dimethylthiazol-2-yl)-2,5-diphenyltetrazolium bromide (MTT) assay. The half inhibitory concentrations (IC_{50} values) obtained from a 72 h incubation assay are listed in Table 1, and representative dose−response curves are provided in the Supporting Information (Figures S17−S19). The bimetallic **1** turned out to be the most potent among all as evidenced by its lowest IC_{50} values (1.3−3.1 μM) against all tested cancer cell lines. In HeLa cells, the antitumor potency of **1** (IC_{50} = 1.3 ± 0.3 μM) is relatively higher as compared to that of the free ligand **L1** (IC_{50} = 23 ± 0.0 μM) and the Pt-Fc hybrids **Pt-Fc-1** (IC_{50} = 4.9 ± 2 μM) and **Pt-Fc-2** (2.8 ± 0.3).[13] Moreover, potency of

1 is 2.7- and 1.6-fold higher as compared to that of cisplatin (3.0 ± 0.1 μM) and oxaliplatin (2.1 ± 0.3 μM) in HeLa cells, respectively. Importantly, comparison of potency of **1** with that of a few previously reported Ru-Fc bimetallic derivatives revealed that **1** is 3−18-fold more potent compared to **Ru1**,[18] **Ru3**,[19] and **Ru4**[20] in A2780 cells. IC_{50} values of **Ru2** and **Ru5** for any of the tested cell lines are not available for comparison purposes. Nevertheless, low or moderate potency was reported for **Ru2** in DL cells and **Ru5** in HT29 cells.[21,22]

To test whether **1** exerted antitumor activity through inhibition of proliferation or induction of cell death, we performed trypan blue dye exclusion assay. HeLa cells were treated with the increasing concentration of **1**, and the number of viable cells present at different time points was counted after staining with trypan blue. As shown in Figure S20, **1** showed a time-dependent antiproliferative effect at 5 and 10 μM concentrations. However, at 20 and 40 μM concentrations, **1** exerted antitumor activity by killing cells, as evidenced from time-dependent reduction in the number of viable cells as compared to that of the initial day.

Comparison of IC_{50} values of **1** in HeLa and A2780 cells with those of its various analogues aids in better understanding of how various functional groups in **1** contribute to its excellent antitumor activity. For example, replacing the CF_3 group with CH_3 in the β-diketonate part (compound **2**) reduces the potency of **1** by several folds. In order to evaluate the importance of the Fc moiety in **1**, we prepared **3** where ferrocene is substituted by a phenyl group. Compound **3** was found to be much less potent compared to **1**, implying that Fc is essential for high potency of the later compound. The observed moderate antitumor activity of **3** (e.g., IC_{50} = 20.7 μM in A2780 cells) compares well with reported antitumor activities of Ru(η^6-arene) compounds bearing purely organic β-diketonato ligands such as [Ru(η^6-arene)Cl(curcuminato)] (IC_{50} = 23.4 μM in A2780 cells) and [Ru(η^6-arene)(PTA)-(4,4,4-trifluoro-1-(4-chlorophenyl)-1,3-butanedionato)] (IC_{50} = 34.8 μM in A2780 cells, PTA = 1,3,5-triaza-7-phosphaadamantane).[12,25] These results confirmed that Fc plays a key role in the potency of **1**. Afterward, we assessed the dependency of the potency on the arene ligand. Replacement of *p*-cymene in **1** with a more hydrophobic hexamethyl benzene afforded **4** which again turned out to be less potent compared to **1**. Substituting the Fc unit in **4** with a phenyl group further reduces the antitumor activity (compound **5**), confirming once again the importance of the Fc unit in the activity of this class of compounds. Furthermore, we observed that activity of **5** can be improved slightly by installing an *m*-CF_3 group at the phenyl ring of the β-diketonate ligand (compound **6**).

Pt drugs cisplatin and carboplatin are commonly used for treatment of ovarian cancers in the clinic.[28] However, the efficacy of Pt therapy is compromised due to inherent and acquired resistance.[15] Therefore, we tested whether our best compound **1** and its analogues **2−5** can overcome Pt resistance in ovarian cancer cells. For this purpose, the RF was calculated as the ratio of IC_{50} values of a compound in cisplatin-resistant A2780Cis cells and in parental cisplatin-sensitive A2780 cells. As noted in Table 1 and presented in Figure 4 (Figures S18 and S19, for dose−response plots), an RF of 8.7 was obtained for cisplatin which is consistent with the previous literature.[13,29] In sharp contrast, all Ru−arene compounds **1−6** presented much lower RF values (RF ≤ 1.5, Figure 4). Intriguingly, along with negligible Pt cross-resistance (RF = 1.2), our best candidate **1** exerted significantly higher potency as

compared to previously reported bimetallics **Ru1, Ru-3**, and **Ru-4** in A2780Cis cells (Table 1).[18−20] Moreover, the lower RF of **1** as compared to that of its parent Pt-Fc derivatives **Pt-Fc-1** and **Pt-Fc-2** (RF = 2.1−2.4) confirmed our hypothesis of passing from Pt to Ru to achieve a bimetallic anticancer hybrid with negligible Pt cross-resistance. Owing to its excellent *in vitro* antitumor potency, compound **1** was selected for *in vivo* evaluation in zebrafish and for in-depth mechanistic studies.

Relative Lipophilicity and Whole Cell Uptake of 1−6

Lipophilicity is one of the very important physicochemical properties of a drug, which plays a crucial role in cellular uptake and antitumor activity.[30] We determined the octanol−water partition coefficients (log *P*) using the traditional shake-flask method, and results are presented in Table 2. The log *P* values of 1−6 range from 0.90 ± 0.01 to 1.19 ± 0.04. The hexamethyl benzene derivatives (**4**−**6**) are slightly more (0.1 to 0.2 log *P* unit) lipophilic compared to *p*-cymene derivatives (**1**−**3**). Nevertheless, the positive log *P* values indicated that these compounds will be able to efficiently enter the cells.

Subsequently, to understand whether the differential IC_{50} values of **1**−**6** arose from varying degrees of cellular accumulation, the whole cell uptake of **1**−**6** was measured by quantifying the total intracellular Ru content using inductively coupled plasma mass spectrometry (ICP−MS). The cellular uptake and intracellular distribution of various Ru compounds were studied previously using confocal microscopy.[9] However, as **1**−**6** are non-luminescent, the cellular uptake and intracellular distribution (*vide infra*) of these classes of compounds were assessed using ICP−MS.[9,13] The accumulation of **1**−**6** in HeLa cells (10 μM, 4 h) is summarized in Table 2. The uptake follows the order **4** > **1** > **2** ~ **6** > **5** > **3**. No linear relation between log *P* and compound accumulation was observed. For instance, despite 1−3 having comparable log *P* values, their cellular accumulation varied drastically; **1** was accumulated 3.5-fold higher than **3**. Comparison of the uptake of bimetallics **1** and **4** (57 ± 9.7 and 89.5 ± 5.3 pmol/10^6 cells, respectively) with that of their respective monometallic phenyl analogues **3** and **5** (16.5 ± 3.2 and 36.4 ± 4.8 pmol/10^6 cells, respectively) suggested that Fc significantly enhances the uptake. Additionally, no direct relationship between the IC_{50} values (Table 1) and cellular uptake (Table 2) of **1**−**6** in HeLa cells was observed. For example, despite cellular accumulation of **1** being 1.6 times lower compared to that of its hexamethyl analogue **4**, the former has a **7** times lower IC_{50} value compared to the latter in HeLa cells.

Ru-Fc Hybrid 1 Is a Non-Toxic Antiangiogenic Small Molecule in Zebrafish Embryos

Our preceding *in vitro* tissue culture data showed that Ru-Fc hybrid **1** is a promising antitumor agent (Figure 5). Angiogenesis is a crucial factor in solid tumor growth and metastasis. Solid tumors induce formation of new blood vessels which are essential for nutrient and oxygen supply to the growing primary solid tumor.[16] In addition to this, tumor cells enter systemic circulation via these intra-tumoral blood vessels and metastasize to other organs.[17] Therefore, inhibition of angiogenesis is an attractive approach to control cancer growth and progression. Indeed, several FDA-approved antiangiogenic agents are routinely used in the clinic as a single agent or in combination with other cytotoxic drugs for treatment of solid tumors.[31] Thus, we intended to explore the role of **1** in angiogenesis and evaluate

the toxicity of **1** *in vivo*. High genetic and physiological similarity between humans and zebrafish[32] and excellent regenerative capacity[33] made zebrafish a preferred model organism in many areas of biomedical research including development of anticancer agents.[34–36] Moreover, high fecundity, optical transparency, and availability of tissue-specific fluorescent reporter lines enable the identification of the effect of candidate drug/small molecules on animal development and organogenesis. Thus, in this study, we used zebrafish embryos to explore the effect of **1** on angiogenesis and its toxicity. A zebrafish sub-intestinal venous plexus (SIVP) development model was used to identify the effect of **1** on angiogenesis.

In zebrafish, the vessels of the SIVP absorb nutrients from the yolk and supply them to the embryo body. Later, in larval and adult zebrafish, the SIVP provides blood supply to the developing digestive system.[37] SIVP formation is initiated from the posterior cardinal vein (PCV) on either side of the yolk sac at around 28 h post-fertilization (hpf) (Figure 5A).[38] A few angiogenic sprouts originate from the PCV at 28 hpf, which grows anteriorly over time, and form the SIVP at 72 hpf (Figure 5a).[38] To explore the effect of **1** on SIVP angiogenesis, zebrafish embryos were treated with DMSO (control) or 20/30/40 μM **1** at 26 hpf, the time before the initiation of SIVP formation, and SIVPs were imaged at 72 hpf with a confocal microscope (Figure 5b). Maximum projections of optical sections of the SIVP revealed a decreased SIVP in **1**-treated embryos as compared to that in the DMSO-treated control at 72 hpf (Figure 5c). Further quantitative analysis of the area covered by the SIVP and the number of compartments in the SIVP found the antiangiogenic activity on embryos treated with 20 μM **1**, and an increased degree of antiangiogenic activity was observed with the increment of the drug concentration (Figure 5d,e), indicating its dose-dependent antiangiogenic effects.

Next, we sought to explore the effect of the Ru-Fc hybrid **1** on the development of zebrafish embryos and viability. Wild-type embryos were treated with DMSO or **1** at 26 hpf, and toxicity was analyzed at 72 hpf. Morphological and viability analysis at 72 hpf of treated embryos showed that **1**-treated animals are 100% viable (Figure 5f) and morphologically indistinguishable from untreated control embryos (Figures 5g and S21) even at 40 μM dose. These results suggest that Ru-Fc hybrid **1** is a non-toxic antiangiogenic molecule.

Interaction of Ru-Fc Hybrid 1 with Biomolecules in Cell Free Settings

DNA and/or proteins are potential intracellular targets of functional Ru(η^6-arene)-based piano-stool anticancer complexes comprising a labile chlorido ligand.[8,39,40] However, a small structural change substantially alters the target specify, cytotoxicity profile, and mechanism of anticancer activity of this class of molecules. For example, DNA is the primary target for RM175 (Figure 1) and structurally related compounds which showed potent *in vitro* and *in vivo* antitumor activity.[11,39] Similar to cisplatin, RM175 preferentially binds to the N-7 position of the guanine base in DNA. In contrast, proteins, enzymes, and DNA are the main targets for the RAPTA class of compounds which exert poor cytotoxicity *in vitro* but potent antimetastatic activity *in vivo*.[8,40] In order to obtain preliminary insights into the possible biomolecular targets, reactivity of 1 toward 9-methylguanine (MG, a model for the guanine base in DNA) and ***N***-acetyl cysteine (NAC, as a model for the thiol side chain in protein) was studied in cell free settings. As shown in Figure 6a, incubation of

a mixture (1:1 molar ratio) 1 and MG in acetonitrile/water (85/15, v/v) led to formation of a new species with time. As expected, electrospray ionization (ESI)-mass spectrometry confirmed the formation of the $[1\text{-Cl} + \text{MG}]^+$ adduct (Figure 6b), suggesting that 1 has the ability to form a covalent adduct with DNA.

Then, interaction of **1** with *N*-acetyl cysteine was studied. For this, compound 1 was treated with increasing amounts of NAC (**1**/NAC, 1/0.05 to 1/1, mol ratio) in an acetonitrile/water mixture, and UPLC was recorded immediately (~2 min post-mixing), and results are presented in Figure S22. The presence of 1 equiv NAC led to immediate disappearance of the peak corresponding to **1** with the appearance of four new peaks in the HPLC chromatogram. Two of those peaks were assigned to ligand **L1** by comparing the HPLC trace of the authentic sample of **L1**. Furthermore, the mass spectrum also showed the presence of free **L1** in the reaction mixture (Figure S22). Rest of the two peaks belonged to the two different NAC adducts of **1** which were identified using MS (Figure S22). These results mirror the reactivity profile of a structurally similar organic *β*-diketone containing a Ru(η^6-*p*-cymene) complex with cystine.[27]

Intracellular Distribution and Genomic DNA Binding of Ru-Fc Hybrid 1

To obtain preliminary insights on possible intracellular targets, organelle distribution of **1** was studied. Cisplatin was included for comparison purposes. HeLa cells were incubated with **1** or cisplatin, cytoplasmic and nuclear fractions were separated, and the amount of metal in each fraction was quantified using ICP−MS. As shown in Figure 7a, cisplatin is equally distributed between the cytoplasm and nucleus in cells. In sharp contrast, the Ru content in the nuclear fraction is ~2.5 times higher compared to the Ru content in the cytoplasmic fraction of **1**-treated cells.

Given the ability of **1** to accumulate in the nucleus and form covalent adducts with MG (vide supra), we speculated that nuclear DNA could be one of the potential targets for **1**. To confirm this, nuclear DNA was isolated from HeLa cells treated with **1** or cisplatin and thoroughly washed to remove any unbound metals, and the amount of metal bound to DNA was quantified using ICP−MS. As shown in Figure 7b, the ability of **1** to metalate DNA is comparable with that of the classical DNA-targeted Pt drug cisplatin. These data strongly suggest that covalent interaction with DNA is one of the possible mechanisms of **1**.

Electrochemical Potential and Generation of ROS

The oxidation potentials (*vs* $Fc^{+/0}$) of **1** and ligand **L1** were found to be 321 and 287 mV, respectively (Figure S23a).[13] Both **L1** and **1** have positive oxidation potentials compared to bare Fc signifying that the 1,3-diketo functionality pulls electrons from the Fc center. Higher oxidation potential of **1** as compared to that of **L1** suggests that coordination with the Ru(II) center makes the Fc moiety even more electron-deficient and subsequently makes its oxidation to the Fc^+ ion even more difficult. Nevertheless, oxidation potential of **1** is below the suggested threshold (i.e., 520 mV *vs* $Fc^{+/0}$) for Fc to Fc^+ oxidation inside cells.[41] Therefore, we expected the Fc moiety in **1** to catalyze the production of highly reactive $HOO^\bullet$ (or $O_2^{\bullet-}$) and $HO^\bullet$ from endogenously produced H_2O_2 through Haber−Weiss-like cycle ending with the Fenton reaction.[21,42,43] To note here, cancer cells produce

high concentrations of H_2O_2 compared to normal cells,[44,45] which has been exploited for selective killing of cancer cells.[14,45–47] Therefore, the ability of **1** to produce ROS in cells was first tested using a broad ROS pro H_2DCF-DA following a previously reported protocol.[13,48] As shown in Figure 8a, significant increase in ROS in **1**-treated HeLa cells was observed only after 1 h incubation with the compound. The amount of intracellular ROS was increased by increasing the incubation time to 4 or 8 h. Interestingly, despite having lower oxidation potential as compared to **1, L1** was unable to elevate the level of intracellular ROS (Figure S23b). This could be attributed to poor cellular uptake of **L1** (pK_a = 6.5) resulting from its ionization and subsequent formation of negatively changed enolate at physiological pH 7.4.[49] Importantly, the monometallic analogue **3** that lacks the Fc moiety was found to produce a significantly lower amount of intracellular ROS as compared to **1**, highlighting the importance of the Fc moiety in production of intracellular ROS (Figure 8a). We note that despite its widespread use for ROS measurement in cells, H_2DCF-DA based ROS assay has several limitations.[50] Therefore, we reassessed the ROS generation ability of **1** using dihydroethidium (DHE) and hydroxyphenyl fluorescein (HPF) as alternative and more selective ROS probes.[51] DHE and HPF are known for their ability to selectively detect intracellular $O_2^{\bullet-}$ and $HO^{\bullet}$ radicals, respectively. Following a previously reported protocol, HeLa cells were treated with 10 μM **1** for 4 h, stained with the ROS probes, and analyzed using flow cytometry[52–54] As shown in Figure 8b,c, the level of $O_2^{\bullet-}$ and $HO^{\bullet}$ radicals in **1**-treated HeLa cells is ~19-fold and ~7-fold higher as compared to that in respective untreated control cells. Both $O_2^{\bullet-}$ and $HO^{\bullet}$ radicals are extraordinarily reactive and expected to execute significant oxidative damage to proteins and DNA in the cells. These results suggest that **1** has the ability to induce oxidative stress in cells, and the same could be a key component in the mechanism of action of compound **1**.

Effect of Ru-Fc Hybrid 1 on Mitochondria and ER

Previous studies from us and others showed that Fc-containing bimetallic compounds have the tendency to accumulate in mitochondria.[13,14] Therefore, to investigate whether a fraction of **1** could potentially accumulate in mitochondria, HeLa cells were treated with 20 μM **1** or 20 μM cisplatin (for comparison), mitochondria were isolated, and metal contents in the mitochondrial fractions were measured. As shown in Figure 9a, ~ 4-fold higher Ru was found in the mitochondria of **1**-treated cells as compared to Pt in the mitochondria of cisplatin-treated cells.

Along with significant mitochondrial accumulation, the ability of **1** to induce oxidative stress prompted us to investigate the effect of **1** on mitochondrial functioning. Mitochondrial damage and/or dysfunction leads to impairment of mitochondrial membrane potential ($\Delta\Psi_m$).[55,56] To this end, a fluorescent $\Delta\Psi_m$ indicator, namely, 5,5,6,6′-tetrachloro-1,1′,3,3′-tetraethyl-imidacarbocyanine iodide (JC-1) dye, in combination with flow cytometry was used to measure $\Delta\Psi_m$ in **1**-treated HeLa cells. In the case of healthy and functional mitochondria with intact $\Delta\Psi_m$, the JC-1 dye accumulates in mitochondria as aggregates and is emitted in the red channel, whereas in case of unhealthy mitochondria with depleted $\Delta\Psi_m$, the JC-1 dye accumulates as monomers inside mitochondria and is emitted in the green channel.[13] It should be noted that since all mechanistic studies were performed in HeLa cells using 24 h incubation assays, the concentrations of **1** for the assays were chosen

to be 1/4 × $IC_{50/24h}$ (10 μM) or 1/2 × $IC_{50/24h}$ (20 μM) or $IC_{50/24h}$ (40 μM) based on the $IC_{50/24h}$ value (38 ± 3 μM) obtained using a 24 h MTT assay (Figure S24). As shown in Figure 9b (Figure S25 for the dot plot), similar to positive control carbonyl cyanide *m*-chlorophenyl hydrazone (CCCP), treatment with **1** led to dramatic decrease in $\Delta\Psi_m$ of HeLa cells even at the ¼ × $IC_{50/24h}$ concentration. Then, we investigated the effect of **1** on the mitochondrial morphology using confocal microscopy. HeLa cells were transiently transfected to label mitochondria with green fluorescent protein (GFP) and treated with **1**. As shown in Figure 9c, mitochondria appeared to be rounded and punctate in cells treated with 1/2 × $IC_{50/24h}$ of **1**, which is in sharp contrast to filamentous and elongated nature of mitochondria in untreated cells. These results indicated that **1** has the ability to target mitochondria and perturb its natural function.

Given the potential inter-connection between ROS production, mitochondrial dysfunction, and ER stress,[6] we studied the effect of **1** on the ER. The ER plays a key role in maintaining calcium storage/homeostasis, lipid biosynthesis, and protein folding/trafficking in cells. Disruptions to any of these functions result in ER stress, leading to accumulation of unfolded proteins which are gradually ubiquitinated for proteasomal degradation.[6] In fact, western blot analysis revealed that similar to a known ER-stress-inducer celastrol,[57] treatment with **1** caused dose-dependent upregulation of unfolded proteins in HeLa cells (Figure 10a). Accumulation of unfolded proteins in ER triggers activation of an adaptive mechanism known as UPR.[6] UPR is initiated mainly through activation of three ER transmembrane proteins, namely, IRE1α, ATF6, and PERK. HeLa cells treated with **1** caused significant upregulation of both IRE1α and ATF6, re-affirming induction of ER stress by **1**. However, upregulation of the PERK arm was not observed as treatment with **1** did not increase the level of the downstream protein p-elF2α of the PERK arm. Similar results were observed for cells treated with the positive control celastrol.[57] Cumulatively, the above-mentioned data strongly suggest that mitochondria and ER are two of the key intracellular targets of compound **1**.

Having established that compound **1** exerts its antitumor activity through ROS generation and mitochondrial dysfunction, we remeasured the antitumor potential of **1** in HeLa and A2780 cells using the non-enzymatic crystal violet (CV) assay (Table S3, Figure S26). It is important to mention that results of an antitumor activity screening can vary dramatically depending on the assay used. For example, the commonly employed MTT assay that we used to determine IC_{50} values (discussed above) reports viability by measuring mitochondrial dehydrogenase activity. Therefore, the results from this assay reflect the effect of a compound on mitochondrial function rather than the effect of the compound on viability or proliferation. By contrast, CV assay is independent of any intracellular enzyme activity and repots the viability by measuring biomass of adherent cells that remain after treatment with a compound. The IC_{50} values determined using 72 h CV assay for **1** were 4.4 ± 1.7 μM on HeLa and 7.2 ± 0.3 μM on A2780 cells. Notably, as presented in Table S3, the IC_{50} values of **1** obtained using CV assay are ~3-fold higher as compared to the IC_{50} values obtained using MTT assay (1.3 μM for HeLa and 2.5 μM for A2780). However, IC_{50} values of cisplatin obtained using CV and MTT assay are comparable (Table S3). These new

results are in line with our expectation as compound **1** exerts its activity by interfering with mitochondrial function.

Mechanism of Cell Death Triggered by Ru-Fc Hybrid

1. After confirming the multi-pronged antitumor mechanism of **1**, which includes generation of ROS, depletion of **ΔΨ**m, induction of ER stress, and covalent adduct formation with nuclear DNA, our next objective was to identify the mechanism of cell death induced by **1**. Apoptosis, necroptosis, autophagy, and paraptosis are the main categories of programed cell death (PCD) mechanisms triggered by DNA damage, oxidative stress, mitochondrial dysfunction, and ER stress.[6,58] First, we performed flow cytometric analysis of HeLa cells using the Annexing-V-FITC (AV, apoptosis marker) and propidium iodide (PI, necrosis marker) dual staining method.[59] While AV binds to phosphatidylserine at the outer leaflet of the plasma membrane of apoptotic cells, PI permeates the compromised plasma membrane and stains the necrotic and late apoptotic cells. Cisplatin (a known apoptosis inducer) and H_2O_2 (a necrosis inducer) were employed as controls for the gating purpose, and results are presented in Figure 11 (Figure S27 for the dot plot). As expected, treatment with cisplatin mainly induced early apoptosis (0.4% AV^+/PI^- in untreated *vs* 13.4% AV^+/PI^- in treated). In sharp contrast, treatment with **1** at a dose of 1/4 × $IC_{50/24h}$ (10 μM) or 1/2 × $IC_{50/24h}$ (20 μM) caused a concentration-dependent increase in AV^-/PI^+ cells (2% in untreated ***vs*** 9% at 10 μM and 15.4% at 20 μM treated), indicating induction of necrosis by **1**. No significant change in the early apoptotic population was noticed at any of the doses. Increasing the dose of **1** to the $IC_{50/24h}$ concentration (40 μM) resulted in further increase in the necrotic population along with the late apoptotic population.

Cleavage of PARP, upregulation of p53, and upregulation of cleaved caspase 3 are important signaling events implicated in apoptotic cell death. As shown in Figure 12a, western blot analysis revealed cleavage of PARP and sharp upregulation of P53 and cleaved caspase 3 in cells treated with the apoptosis-inducer cisplatin (10 μM). In contrast, none of these apoptosis markers were upregulated in the cells treated with **1** (1/4 × IC_{50} to IC_{50} concentrations of **1**, 24 h). Cumulatively, these data confirmed that apoptosis is not the primary mechanism of cell death induced by **1**.

Autophagy is another type of programed cell death which is regulated via conversion of LC3-I to LC3-II protein.[60] Western blot analysis showed no increase in the ratio of LC3-II/LC3-I in cells treated with **1** (Figure 12b). Moreover, acridine orange assay revealed that treatment with **1** did not cause formation and promotion of acidic vesicular organelles that are one of the important features of autophagy (Figure S28).[61,62] Based on these results, the possibility of autophagic cell death by **1** was ruled out.

Our recently reported Pt-Fc anticancer hybrid **Pt-Fc-2** induces severe ER dilation accompanied with progressive cytosolic vacuolization in cells, which are important hallmarks of paraptosis-like cell death.[13] However, although **1** caused ER stress (vide supra), ER dilation and/or vacuole formation were not observed in **1**-treated HeLa cells (Figure S29); thus, induction of paraptosis-like cell death is highly unlikely.

Induction of necrosis by **1** was evident from the flow cytometry experiments (Figure 11). Therefore, next, we investigated whether **1** elicits programed necrosis termed necroptosis. The core cellular events associated with the necroptosis pathway involve upregulation of the receptor interacting protein (RIP) kinases RIP1 and RIP3, leading to stimulation of mixed lineage kinase-like (MLKL) protein.[60,63] Western blot analysis confirmed that similar to a known necroptosis-inducer shikonin,[64] treatment with **1** increased the expression level of RIP1 and RIP3 in HeLa cells (Figure 12c), confirming necroptosis-mediated cell death evoked by **1**.

Apart from ROS, mitochondrial damage, and ER stress, necroptotic cell death can also occur through hyper-activation of PARP. PARP is a nuclear enzyme involved in the DNA repair process. Severe damage to DNA results in upregulation of PARP which activates RIP1.[65,66] As shown in Figure 12a, we observed significant upregulation of PARP in HeLa cells treated with **1**, suggesting severe DNA damage caused by **1**. This is in line with our expectation as an appreciable amount of **1** accumulates in the nucleus, and **1** has the ability to metalate DNA and produce ROS (discussed earlier). This data suggests that activation of PARP is one of the upstream events involved in RIP1-mediated necroptosis induced by **1**.

Recent reports have suggested that the downstream event of necroptosis involves formation and opening of the mitochondrial permeability transition pore (MPTP), which results in mitochondrial dysfunction, bioenergetics disbalance, and ATP depletion.[67] Following activation of RIP1/RIP3 and MLKL, opening of the MPTP occurs via two pathways: (i) calcium (Ca^{2+}) overload in mitochondria and/or (ii) Bax- and Bak (non-oligomerized form)-mediated alteration of mitochondrial outer membrane permeability.[67] In fact, HeLa cells treated with **1** showed ~5-fold increase in the mitochondrial Ca^{2+} level as compared to the untreated control (Figure 12d). To test whether Bax and Bak play any role in **1**-mediated necroptosis, cytotoxicity studies were performed using a wild-type murine embryonic fibroblast (MEF-Bax/Bak$^{+/+}$) and its corresponding Bax/Bak double knocked-out (MEF-Bax/Bak$^{-/-}$) cell lines. As show in Figure 12e, The IC_{50} values of **1** are statistically similar in MEF-Bax/Bak$^{+/+}$ and MEF-Bax/Bak$^{-/-}$ cells, suggesting that **1**-induced necroptosis is independent of Bax and Bak activity (see Figure S30 for dose−response plots). A summary of the anticancer mechanism of action of **1** is presented in Figure 12f. Interestingly, in line with previous reports,[13,68] the IC_{50} values for apoptosis-inducing drug cisplatin are 2.5-fold higher in MEF-Bax/Bak$^{-/-}$ cells as compared to those in the WT MEF-Bax/Bak$^{+/+}$ cells. This is expected as Bax and Bak are key regulators of apoptosis. Along with understanding the mechanism of action, these results have high clinical significance because pro-apoptotic proteins p53, Bax, and Bak are downregulated or inactivated in many cancers, making them nonresponsive to apoptotic drugs.[68−70] Based on the results, we conclude that 1 is capable of circumventing apoptosis resistance caused by dysfunctional apoptosis machinery in many solid tumors.

Conclusions

In summary, this article presents design, synthesis, preliminary SAR analysis, and in-depth biological evaluation of a novel Ru-Fc bimetallic antitumor agent **1** with potent *in vitro* anticancer activity and *in vivo* antiangiogenic activity. Compound **1** possesses good stability

in water (with 100 mM NaCl) and in cell culture medium and exerted low micromolar IC_{50} values (1.3 to 3.1 μM) against different cancer cell lines. Notably, along with low Pt cross-resistance (RF = 1.2), **1** presented significantly higher antitumor potency as compared to previously reported bimetallic Ru-Fc compounds in cisplatin-resistant A2780Cis cells. The lower RF of **1** when compared to that of its parent Pt-Fc derivatives (RF = 2.1−2.4) confirmed our hypothesis that moving from Pt to Ru significantly improves the Pt cross-resistance profile of Fc-appended bimetallic anticancer agents. Five analogues (**2**−**6**) of **1** were also synthesized, fully characterized, and used for SAR analysis that aids in better understanding of how various functional groups, specifically Fc, CF_3, and arene, contribute to the excellent potency of our best candidate **1**. Besides the excellent antitumor activity, our *in vivo* analysis identified that **1** has potent antiangiogenic properties. Excessive blood vessel growth is essential for tumor growth and metastatic spread.[16,17] Thus, in recent years, antiangiogenic molecules have received special attention in managing tumor growth and metastasis in solid tumors.[31,71] Antitumor and antiangiogenic properties of **1** indicate that this molecule will be an excellent candidate to manage solid cancer. Furthermore, **1** did not show any visible toxic effects on embryonic development and on viability of zebrafish embryos at 40 μM, evidencing the excellent *in vivo* safety profile of this agent. To the best of our knowledge, this is the first report on evaluation of toxicity and antiangiogenic activity of a Ru(II)−arene-containing Ru-Fc bimetallic conjugate. Our in-depth mechanistic studies identified nuclear DNA, mitochondria, and ER as potential intracellular targets of **1**. Along with DNA damage, **1** led to generation of intracellular ROS, depletion of $\Delta\Psi_m$, and induction of ER stress. This multi-pronged mechanism of action of **1** in cancer cells triggers PARP-dependent necroptosis-mediated PCD which is independent of Bax and Bak. This study will help pave the way to the development of a novel class of bimetallic anticancer antiangiogenic agents.

Experimental Section

Materials

Chemicals and solvents obtained from commercial suppliers were of reagent grade quality or better and used without further purification. Solvents were used as received or dried over molecular sieves. All preparations were carried out using standard Schlenk techniques. Starting materials such as the dichloro(*p*-cymene)ruthenium(II) dimer, dichloro(hexamethylbenzene)-ruthenium(II) dimer, ethyl trifluoroacetate, acetyl ferrocene, and **L3** were purchased from Sigma-Aldrich. The ligands **L1**,[13] **L2**,[13,23] and **L4**[24] and Pt-Fc derivatives **Pt-Fc-1** and **Pt-Fc-2**[13] were synthesized by following the reported procedure, and spectroscopic data matched with those reported previously. The purity of all compounds used for biological test is ≥95% determined using elemental microanalysis and UPLC.

Instrumentation and Methods

NMR spectroscopic measurements were done using Bruker 800 MHz and Varian 600 MHz spectrometers at 22 °C in the NMR facility, TIFR Mumbai. All the measurements were carried out using deuterated solvents, and chemical shifts δ are reported in ppm (parts per million), and coupling constants J are given as absolute values in hertz. The residual solvent peaks were used as an internal reference for ^1H and ^{13}C NMR spectra, and chemical

shifts are expressed relative to tetramethylsilane ($SiMe_4$, $\delta = 0$ ppm). Abbreviations for the peak multiplicities are as follows: s (singlet), d (doublet), dd (doublet of doublets), t (triplet), q (quartet), m (multiplet), and br (broad). Mass spectra were recorded on a Bruker ultrafleXtreme MALDI-TOF mass spectrometer. Simulated mass spectra were obtained from SISweb (https://www.sisweb.com/mstools.htm). Elemental microanalyses were performed on a Thermo Fisher FLASH2000 CHNS/O analyzer. ICP−MS measurements were carried out using an Agilent 7900 ICP−MS. Analytical HPLC was performed using a Shimadzu-Nexera X2 UPLC system fitted with a C18 reverse-phase column (Waters C18, 2.1 mm × 50 mm, 1.7 μm). The flow rate was 0.4 mL min^{-1}, and UV absorption was measured at 220 and/or 254 nm.

Synthesis and Characterization: General Procedure for Synthesis of 1−6

In a 100 mL round bottom flask, dimer $[(\eta^6\text{-arene})RuCl_2]_2$ (l equiv), β-diketone (2 equiv), and sodium methoxide (2.2 equiv) as the base were dissolved in 20 mL of a 10% methanol/DCM mixture. The reaction mixture was refluxed for 4 h, and later, the solvent was removed. DCM was added to precipitate the byproduct NaCl and filtered through Celite. The solution was concentrated to 1−2 mL, and this concentrated solution was added dropwise to 50 mL of *n*-hexane, which started to give a precipitate. The precipitate was filtered and dried in high vacuum. Precipitation in *n*-hexane was repeated a few times for removing excess β-diketone ligands, if any. Products were characterized by ^{1}H NMR, ^{13}C NMR, and MS analysis. Purity of compounds **1−6** is ≥95% determined using elemental microanalysis and UPLC (UPLC traces presented in the Supporting Information).

Compound 1—Reagents used: $[(\eta^6\text{-}\boldsymbol{p}\text{-cymene})RuCl_2]_2$ (190.9 mg, 0.31 mmol), 4,4,4-trifluoro-1-ferrocenylbutane-1,3-dione (**L1**, 202.5 mg, 0.63 mmol), and NaOMe (1.4 mL, 0.5 M, 0.69 mmol). Compound **1** was obtained as a brownish-red powder (yield: 323 mg, 85%). ^{1}H NMR (600 MHz, $CDCl_3$): δ 5.71 (s, 1H), 5.61 (d, J = 5.2 Hz, 1H), 5.53 (d, J = 5.2 Hz, 1H), 5.26 (t, J = 4.7 Hz, 2H), 4.86 (s, 1H), 4.62 (s, 1H), 4.52 (s, 1H), 4.45 (s, 1H), 4.23 (s, 5H), 2.97 (sept, 1H), 2.26 (s, 3H), 1.41 (dd, J = 6.9, 4.5 Hz, 6H). ^{13}C{^{1}H} NMR (201 MHz, $CDCl_3$): δ (ppm) 191.0, 165.8, 122.2, 119.1, 117.7, 99.4, 97.6, 92.0, 83.96, 83.2, 79.3, 78.9, 77.3, 77.1, 77.0, 72.5, 72.3, 70.9, 69.2, 68.8, 31.1, 22.5, 22.4, 17.8. ESI-MS (pos. detection mode, MeOH): m/z (%) 559.01 (100) $[M - Cl]^+$, calcd m/z for $[M - Cl]^+$ 559.01. t_R (RP-HPLC) = 3.64 min. Anal. Calcd for $C_{24}H_{24}ClF_3FeO_2Ru\cdot(C_6H_{14})_{0.2}$: C, 49.53; H, 4.42; Found: C, 49.52; H, 4.39.

Compound 2—Reagents used: $[(\eta^6\text{-}p\text{-cymene})RuCl_2]_2$ (190.9 mg, 0.31 mmol), 1-ferrocenylbutane-1,3-dione (**L2**, 168.8 mg, 0.63 mmol), and NaOMe (1.4 mL, 0.5 M, 0.69 mmol). Compound **2** was obtained as a brown powder (yield: 280.5 mg, 81%). ^{1}H NMR (600 MHz, $CDCl_3$): δ 5.52 (d, J = 5.2 Hz, 1H), 5.46 (d, J = 5.2 Hz, 1H), 5.40 (s, 1H), 5.20 (d, J = 4.7 Hz, 1H), 5.16 (d, J = 4.7 Hz, 1H), 4.80 (s, 1H), 4.58 (s, 1H), 4.35 (s, 1H), 4.32 (s, 1H), 4.20 (s, 5H), 2.99 (sept, 1H), 2.26 (s, 3H), 2.04 (s, 3H), 1.41 (t, J = 5.7 Hz, 6H). ^{13}C{^{1}H} NMR (201 MHz, $CDCl_3$): δ (ppm) 183.63, 183.05, 97.66, 96.93, 95.04, 83.45, 83.01, 80.34, 78.04, 77.90, 70.53, 69.77, 68.63, 67.55, 39.73, 39.62, 39.52, 39.42, 39.31, 30.36, 27.17, 22.05, 21.99, 17.15. ESI-MS (pos. detection mode, MeOH): m/z (%) 505.04

(100) $[M - Cl]^+$, calcd *m*/*z* for $[M - Cl]^+$ 504.04. t_R (RP-HPLC) = 3.15 min. Anal. Calcd for $C_{24}H_{27}ClFeO_2Ru\cdot(H_2O)_{0.8}$: C, 52.01; H, 5.20. Found: C, 52.06; H, 5.02.

Compound 3—Reagents used: $[(\eta^6\text{-}p\text{-cymene})RuCl_2]_2$ (190.9 mg, 0.31 mmol), 4,4,4-trifluoro-1-phenylbutane-1,3-dione (L3, 135.0 mg, 0.63 mmol), and NaOMe (1.4 mL, 0.5 M, 0.69 mmol). Compound **3** was obtained as a brown powder (271.9 mg, yield: 87%). ^{1}H NMR (600 MHz, $CDCl_3$): δ 7.86 (d, J = 7.4 Hz, 2H), 7.51 (t, J = 7.4 Hz, 1H), 7.41 (t, J = 7.8 Hz, 2H), 6.19 (s, 1H), 5.63 (d, J = 5.2 Hz, 1H), 5.60 (d, J = 5.2 Hz, 1H), 5.35 (d, J = 4.7 Hz, 1H), 5.33 (d, J = 4.7 Hz, 1H), 2.98 (sept, 1H), 2.30 (s, 3H), 1.39 (t, J = 5.7 Hz, 6H). ^{13}C{^{1}H} NMR (201 MHz, DMSO-d_6): δ (ppm) 185.21, 167.76, 167.60, 136.51, 132.91, 128.85, 127.46, 98.80, 97.91, 90.55, 83.44, 82.92, 78.64, 78.32, 39.83, 39.73, 39.62, 39.52, 39.42, 39.31, 39.21, 30.42, 21.88, 21.84, 17.48. ESI-MS (pos. detection mode, MeOH): *m*/*z* (%) 451.04 (100) $[M - Cl]^+$, calcd *m*/*z* for $[M - Cl]^+$ 451.04. t_R (RP-HPLC) = 3.10 min. Anal. Calcd for $C_{20}H_{20}ClF_3FeO_2Ru\cdot(H_2O)_{1.2}$: C, 47.33; H, 4.45. Found: C, 47.14; H, 4.28.

Compound 4—Reagents used: $[(hexamethylbenzene)RuCl_2]_2$ (208.4 mg, 0.31 mmol), **L1** (202.5 mg, 0.63 mmol), and NaOMe (1.4 mL, 0.5 M, 0.69 mmol). Compound **4** was obtained as a brown powder (353.8 mg, yield: 91%). ^{1}H NMR (600 MHz, CD_2Cl_2): δ 5.68 (s, 1H), 4.84 (s, 1H), 4.72 (s, 1H), 4.52 (s, 1H), 4.49 (s, 1H), 4.20 (s, 5H), 2.09 (s, 18H). ^{13}C{^{1}H} NMR (201 MHz, DMSO-d_6): δ (ppm) 190.17, 91.11, 90.03, 79.21, 72.43, 72.18, 70.25, 69.47, 68.02, 39.72, 39.62, 39.52, 39.42, 39.32, 14.69 ESI-MS (pos. detection mode, MeOH): *m*/*z* (%) 587.04 (100) $[M - Cl]^+$, calcd *m*/*z* for $[M - Cl]^+$ 587.04. t_R (RP-HPLC) = 3.78 min: 302.13, 509.91. Anal. Calcd for $C_{26}H_{28}ClF_3FeO_2Ru\cdot(H_2O)$: C, 48.80; H, 4.73. Found: C, 48.66; H, 4.44.

Compound 5—Reagents used: $[(hexamethylbenzene)RuCl_2]_2$ (208.4 mg, 0.31 mmol), **L3** (134.4 mg, 0.63 mmol), and NaOMe (1.4 mL, 0.5 M, 0.69 mmol). Compound **5** was obtained as a brown powder (186.3 mg, yield: 85%). ^{1}H NMR (600 MHz, CD_2Cl_2): δ 7.91 (d, J = 7.4 Hz, 2H), 7.55 (t, J = 7.4 Hz, 1H), 7.45 (t, J = 7.8 Hz, 2H), 6.16 (s, 1H), 2.10 (s, 18H). ^{13}C{^{1}H} NMR (201 MHz, DMSO-d_6): δ (ppm) 184.71, 167.36, 136.64, 132.72, 128.90, 127.07, 90.37, 39.72, 39.62, 39.52, 39.42, 39.32, 14.78. ESI-MS (pos. detection mode, MeOH): *m*/*z* (%) 479.07 (100) $[M - Cl]^+$, calculated *m*/*z* for $[M - Cl]^+$ 479.07. t_R (RP-HPLC) = 3.35 min. Anal. Calcd for $C_{22}H_{24}ClF_3O_2Ru\cdot(H_2O)_{0.25}$: C, 50.97; H, 4.76. Found: C, 50.90; H, 4.66.

Compound 6—Reagents used: $[(hexamethylbenzene)RuCl_2]_2$ (208.4 mg, 0.31 mmol), 1-[3-(trifluoromethyl)phenyl]butane-1,3-dione (**L4**, 143.8 mg, 0.63 mmol), and NaOMe (1.4 mL, 0.5 M, 0.69 mmol). Compound **6** was obtained as a brown powder (297 mg, yield: 90%). ^{1}H NMR (600 MHz, CD_2Cl_2): δ 8.14 (s, 1H), 8.05 (d, J = 7.9 Hz, 1H), 7.70 (d, J = 7.8 Hz, 1H), 7.54 (t, J = 7.8 Hz, 1H), 5.79 (s, 1H), 2.14 (s, 3H), 2.08 (s, 18H). ^{13}C{^{1}H} NMR (201 MHz, DMSO-d_6): δ (ppm) 188.84, 174.97, 139.06, 130.39, 129.75, 129.12, 127.24, 122.83, 95.18, 89.85, 39.83, 39.73, 39.62, 39.52, 39.42, 39.31, 39.21, 28.31, 14.68. ESI-MS (pos. detection mode, MeOH): *m*/*z* (%) 493.09 (100) $[M - Cl]^+$, calcd *m*/*z* for $[M - Cl]^+$ 493.09. t_R (RP-HPLC) = 3.41 min. Anal. Calcd for $C_{23}H_{26}ClF_3O_2Ru\cdot(H_2O)_{0.5}$: C, 51.45; H, 5.07. Found: C, 51.30; H, 4.82.

X-ray Crystallography

The X-ray diffraction data for compound **6** were collected at 293 K temperature using a Rigaku Xtal LAB X-ray diffractometer system equipped with a charge-coupled device (CCD) area detector (Cu Kα; radiation λ = 0.710 73 Å). The data images were reintegrated and reduced using CrysAlis^{Pro} (Rigaku Oxford Diffraction) with a narrow frame algorithm. The crystal structure was solved by the direct methods in SHELXTL[72] and refined by the full matrix least-squares method on F^2 (SHELXL-2014)[73] using Olex2 software.[74]

Stability in DMSO and Aqueous Media

Stability of **1** in DMSO and in aqueous media in the presence of the physiologically relevant Cl^- ion was determined using ^{1}H NMR. To a ~2 mM solution of 1 in DMSO-d_6 was added a 666 mM NaCl solution in D_2O in order to get a final concentration of 100 mM NaCl solution in DMSO/D_2O (85/15, v/v), and ^{1}H NMR was recorded at regular intervals up to 48 h. Further increasing the D_2O content led to precipitation of the compound.

Reversible Aquation and Anation

To a ~2 mM solution of **1** in DMSO-d_6 was added D_2O to make a solution of **1** in the DMSO/D_2O mixture (90/10, v/v). ^{1}H NMR spectra was recorded at 2 and 10 min thereafter, until full conversion of chloro species to aqua species was obtained. Immediately after 10 min, 666 mM NaCl solution in D_2O was added to the NMR tube to get resulting 100 mM NaCl in DMSO/D_2O (85:15 v/v), and the ^{1}H NMR spectrum was recorded thereafter at regular intervals up to 60 min.

Stability in RPMI-1640 Cell Culture Medium

Stability of **1** in cell culture medium RPMI was studied using UPLC. Carbamazepine was added as an internal standard. Freshly prepared stock solutions of carbamazepine (10 μL, 2 mM stock solution in DMSO) and **1** (20 μL, 5 mM stock solution in DMSO) were added to 480 μL of RPMI in a 1.5 mL tube. The resulting mixture was incubated at 37 °C in a rotor at 20 rpm, and 1 μL from that mixture was injected into the UPLC column at regular intervals up to 24 h. The ratio of the peak intensity (**1**/carbamazepine) observed at 254 nm was plotted as a percentage of the ratio at t = 0 with time to obtain the stability plot of **1** in RPMI. UPLC method: a linear gradient of Millipore water with 0.1% trifluoroacetic acid (TFA) (A) and acetonitrile (B, Sigma-Aldrich HPLC-grade) was used. t = 0.01 min, 0% B; t = 2 min, 0% B; t = 2.13 min, 25% B; t = 2.25 min, 40% B; t = 2.5 min, 54% B; t = 3 min, 71% B; t = 3.7 min, 85% B; t = 4.71 min, 92% B; t = 4.81 min, 100% B. The flow rates were 0.4 mL min^{-1}, and UV absorption was measured at 254 nm. The experiment was repeated two times with three replicates each time.

Cell Culture

Cell lines were purchased from ATCC and ECAAC. HeLa (human cervical carcinoma) cells were cultured in Dulbecco's modified Eagle's medium (DMEM) with 10% FBS and 1% penicillin/streptomycin. A2780 (human ovarian carcinoma) and A2780Cis (cisplatin-resistant A2780) were cultured in RPMI medium with 10% FBS and 1% penicillin/streptomycin. The A2780Cis cell line was treated for 3 days every week with 2 μM cisplatin.

Bax-Bak-DKO mouse embryonic fibroblasts (MEFs) and Bax-Bak-WT MEFs were cultured in Iscove's modified Dulbecco's *medium* with 10% FBS and 1% penicillin/streptomycin. The cells were maintained in an incubator at 37 °C with 5% CO_2.

Cell Viability Assays

The effect of compounds on cell viability was determined using a colorimetric MTT and non-enzymatic CV assay. Cells (3×10^3 cells/well in 100 μL of medium) were seeded in a 96-well plate and allowed to grow overnight. The following day, stock solutions of the desired concentration of compounds 1−6 in DMSO were freshly prepared by weighing the compounds using a microbalance (Mettler Toledo XP6). The concentration of stock solutions was reconfirmed by measuring the Ru content using ICP−MS. Then, the fresh stock solutions were serially diluted using cell culture medium, and 100 μL of medium containing a known concentration of compounds was added to each well. Cisplatin stock solution was prepared freshly in phosphate buffered saline (PBS). The concentration of the stock solution was chosen in such a way that the final DMSO concentration never exceeded 0.1%. After the required incubation time, the medium was aspirated, and 200 μL of fresh medium containing MTT (0.5 mg mL^{-1}) was added to each well, and the plate was incubated for 3 h. The medium was then removed, and the resulting purple formazan crystals were dissolved in DMSO (180 μL/well). The absorbance of the solution in each well was read at 570 nm using a BioTek Cytation 5 microplate reader. Absorbance values were normalized with respect to untreated control wells and plotted as a concentration of test compound versus % cell viability. IC_{50} values were obtained from the resulting dose-dependence curves. The reported IC_{50} values are the average from at least three independent experiments, each of which consisted of either three or six replicates.

For CV assay, cells were seeded and treated with test compounds as described for MTT assay. After incubation, wells were washed with 200 μL of PBS per well, and then, cells were fixed with 50 μL of 4% paraformaldehyde (w/v, in PBS) for 15 min followed by washing with 200 μL of PBS/well. Cells were then permeabilized with 50 μL/well of 0.01% Triton X (v/v, in PBS) for 5 min. Then, Triton X was washed again washed with PBS (2 × 200 μL). Plates were then incubated with 50 μL/well of 0.04% (w/v, in PBS) CV solution for 60 min. Then, plates were thoroughly washed with normal tap water (four times) with proper care and kept overnight to dry. After drying, the CV was dissolved with 96% ethanol (200 μL/well), and then, absorption was measured at 570 nm using a BioTek Cytation 5 microplate reader.

Cell Proliferation Using Trypan Blue Assay

HeLa cells were seeded in 24-well plates. Next day, some of the wells were trypsinized, and cells were collected and stained with trypan blue, and live cells were counted using a hemocytometer to obtain the number of cells at 0 h. On the same day, some wells were left untreated, and other wells were treated with different concentrations of **1**. The number of viable cells in each well was counted at 24, 48, 72, 96, and 120 h post-incubation. The number of viable cells was plotted against incubation time using Origin to obtain the proliferation plot in the absence and presence of different concentrations of **1**.

Measurement of the Water/Octanol Partition Coefficient (log *P*)

The log *P* values for compounds **1**−**6** were determined using the shake-flask method. Octanol-saturated water (OSW) and water-saturated octanol (WSO) were prepared by shaking a 1:1 mixture of 1-octanol and water for 24 h, followed by separation of each layer using a separating funnel. Stock solutions of **1**−**6** (*ca.* 2 mM) were made in DMSO, and 25 μL was added to 2 mL of WSO containing 100 mM NaCl. 600 μL of this solution was added to 600 μL of OSW in a 2 mL tube and shaken for 2 h at 37 °C using an automated shaker (800 rpm). 600 μL of this solution was added to 600 μL of OSW and stirred for 2 h at 37 °C at 800 rpm. The aqueous layer was carefully separated from the octanol layer. The Ru content, [Ru], was quantified in aqueous layers before and after partition using ICP−MS. log *P* was calculated using the following equation.

$$\log P = \log\left(\frac{[\mathrm{Ru}]_{\text{in water layer before partition}} - [\mathrm{Ru}]_{\text{in water layer after partition}}}{[\mathrm{Ru}]_{\text{in water layer after partition}}}\right)$$

Whole Cell Uptake

Cells (2×10^6 cells) were seeded in a 60 mm culture plate and allowed to grow overnight. Medium was aspirated, and 3 mL of fresh medium containing the test compound (10 μM) was added and incubated for 4 h. Then, medium was aspirated and washed with PBS (3 × 3 mL), and cells were detached using trypsin and counted. Cells were then pelleted using centrifugation (1200 rpm, 6 min) and digested with HNO_3 (70%, 400 μL) and H_2O_2 (30%. 400 μL) at room temperature for 4 days. The amount of the Ru content in each sample was measured using ICP−MS. The Ru content was normalized with respect to the total number of cells in each sample. The experiment was performed three times each having three replicates.

In Vivo Assays Using Zebrafish

Zebrafish Maintenance—Wild-type AB and transgenic *Tg(etv2:EGFP)* zebrafish[75] (*Danio rerio*) were maintained in a state-of-the-art fish aquarium. Water temperature, pH, and conductivity were maintained as described.[76]

Ethics Statement—Less than 5 days post-fertilization (dpf), zebrafish embryos were used in this study. Zebrafish maintenance and experimentation on zebrafish embryos were performed following the Committee for the Purpose of Control and Supervision of Experiments on Animals (CPCSEA), Government of India, and the Institutional Animal Ethics Committee (IAEC), ARI guidelines.

Drug Treatment to Zebrafish Embryos—Compound **1** was dissolved in DMSO at the 5 mM concentration (stock). For the treatment, 5 mM stock solution in DMSO was diluted in embryo water (E3) to avail a 20, 30, or 40 μM final concentration of RuFc**1**. To explore the effect of **1** on zebrafish SIVP angiogenesis, four 26 hpf Tg(etv2: EGFP) transgenic embryos were placed in 1 mL of E3 medium supplemented with 20, 30, or 40 μM RuFc**1** or DMSO (vehicle control, 10 μL DMSO/mL E3 medium) and raised to 72 hpf in a 28 °C incubator.

For toxicity and viability analysis, 10 no background 26 hpf wild-type embryos were placed in 5 mL of E3 medium supplemented with 20, 30, or 40 μM RuFc**1** or DMSO (vehicle control, 10 μL DMSO/ mL E3 medium) and raised to 72 hpf in a 28 °C incubator.

Confocal Microscopy and Morphological Analysis of Zebrafish Embryos—For whole-mount SIVP imaging, 72 hpf drug- or DMSO-treated Tg(etv2: EGFP) transgenic anesthetized embryos [with 0.04% tricaine (w/v)] were mounted on a glass-bottom plate in 0.5% low-melting-point agarose in E3 medium. Optical sections of SIVPs were imaged with a Leica SP8 confocal microscope. Images were processed with the help of Leica LAS AF Lite and Gimp software. The area covered by the SIVP and the presence of vessel compartments in each SIVP were analyzed using ImageJ software. For each treatment condition, 20 animals at least from 4 independent experiments were considered for the SIVP development analysis.

Brightfield Imaging and Analysis of Zebrafish Embryos—For viability study, drug- or DMSO-treated live animals were counted at 72 hpf. For morphological analysis, brightfield images of drug- or DMSO-treated live embryos were captured at 72 hpf using a Leica M205 FA stereoscope. For each treatment condition, 40 animals from 4 independent experiments were considered for the viability and morphological analysis.

Statistical Analysis of Data Derived from the Experiments on Zebrafish Embryos—Embryo viability and SIVP complexity were analyzed by a two-tailed Student's *t*-test. Prism7 software was used for data processing. Data are represented in the mean ± s.e.m. format, and *P* values (*$p \leq 0.05$, **$p \leq 0.01$, ***$p \leq 0.001$) were calculated accordingly.

Reaction of 1 with 9-Methylguanine—Compound **1** (100 μM) and 9-methylguanine (100 μM) were mixed in an acetonitrile/water mixture (85:15, v/v) and incubated at 37 °C in a rotor at 30 rpm, and 3 μL from that mixture was injected into the UPLC column at regular time intervals up to 48 h. UPLC method: a linear gradient of Millipore water with 0.1% TFA (A) and acetonitrile (B, Sigma-Aldrich HPLC-grade) was used. $t = 0.01$ min, 0% B; $t = 1.15$ min, 0% B; $t = 1.25$ min, 28% B; $t = 1.3$ min, 36% B; $t = 1.7$ min, 40% B; $t = 2$ min, 56% B; $t = 2.5$ min, 64% B; $t = 3.2$ min, 70% B; $t = 4.55$ min, 70% B; $t = 4.6$ min, 100% B. The flow rates were 0.4 mL min^{-1}, and UV absorption was measured at 254 nm. The mixture obtained after 36 h of incubation was used for LC−MS analysis (ESI positive mode), and the molecular ion peaks of the Ru−guanine adduct were assigned.

Reaction of 1 with N-Acetyl Cysteine—A 100 μM solution of compound **1** was made in acetonitrile (total volume = 500 μL) in a 1.5 mL tube. To this tube, incremental amounts (5, 15, 20, 20, 40 μL) from a stock solution of *N*-acetyl cysteine in water (500 μM) were added sequentially. After each addition and subsequent mixing for 2 min, 1 μL from the mixture were injected in to the UPLC column, and all the UPLC traces were stacked plotted together. The resultant stoichiometric equivalents of NAC/**1** during the experiment increased from 0, 0.05, 0.2, 0.4, 0.6 and finally to an equimolar mixture, respectively. In order to confirm the cleavage of **L1** from compound **1** as a result of reaction with NAC, the UPLC

trace of ligand **L1** was also co-stacked. UPLC method: a linear gradient of Millipore water with 0.1% TFA (A) and acetonitrile (B, Sigma-Aldrich HPLC-grade) was used. ***t*** = 0.01 min, 0% B; *t* = 2 min, 0% B; *t* = 2.13 min, 25% B; *t* = 2.25 min, 40% B; *t* = 2.5 min, 54% B; *t* = 3 min, 71% B; *t* = 3.7 min, 85% B; *t* = 4.71 min, 92% B; *t* = 4.81 min, 100% B. The flow rates were 0.4 mL min^{-1}, and UV absorption was measured at 254 nm. The formation of Ru−NAC adducts was confirmed by analyzing the 1:1 mixture of NAC/1 using MALDI mass spectrometry.

Intracellular Organelle Distribution of 1—HeLa cells (5×10^6) were seeded in a 100 mm culture plate and allowed to grow overnight. Then, the cells were treated with 10 μM compound **1** or 10 μM cisplatin (as control) for 24 h. Medium was aspirated, plates were washed with 3 × 5 mL of PBS, and cells were collected by trypsinization and pelleted. Cells were then resuspended in 1 mL of PBS, counted, and re-pelleted. The nuclear and cytoplasmic fractions were isolated using a NEPER kit (Thermo Fisher) following the manufacturer protocol. The protein content and metal content in each fraction were measured using bicinchoninic acid assay and ICP−MS, respectively.

For quantifying accumulation of compounds in mitochondria, a similar protocol was followed after isolating and purifying the mitochondria using a mitochondrial isolation kit (Thermo Fisher) as per manufacturer's instructions. The metal content was normalized with the protein content from the respective samples. Each of the experiments was conducted three times with three or more replicates.

DNA Metalation—HeLa cells (5×10^6) were seeded in a 100 mm culture plate and allowed to grow overnight. The cells were treated with 20 μM compound **1** or cisplatin for 24 h. Then, medium was aspirated, and cells were washed with PBS (3 × 5 mL), and then, DNAzol (1 mL, genomic DNA isolation reagent, Thermo Fisher) was added to the Petri dish, and the lysate was transferred into a 1.5 mL tube. The DNA was precipitated with pure ethanol (0.5 mL), washed with 75% ethanol (0.75 mL × 3), and re-dissolved in 500 μL of 8 mM NaOH. The DNA concentration was determined using a SpectraMax QuickDrop Micro-Volume Spectrophotometer, and the respective metal content was measured using ICP-MS. The experiment was performed in triplicate.

Cyclic Voltammetry of Compound 1—Compound **1** was dissolved in acetonitrile (final conc. ~1.25 mM), and NEt_4BF_4 (0.1 M) was added as the electrolyte; scan rate, 50 mV/s; reference electrode, Ag/ AgCl (1 M KCl); working electrode, Pt; auxiliary electrode, a Pt wire was used. Reduction potential with reference to Fc ($Fc^{+/0}$) was calculated by subtracting 390 mV from all potential values. The arrow indicates the initial direction of the scan. All measurements were done at 298 K and under atmospheric conditions.

Intracellular ROS Quantification—HeLa cells (10×10^3/wells in 100 μL) were seeded in black glass-bottom 96-well plate and allowed to grow overnight. The cells were treated with 10 μM test compounds for required periods. After the incubation time, the medium was aspirated, and the cells were washed with PBS (100 μL × 2) and stained with 10 μM H_2DCF-DA for 30 min. The cells were washed again with PBS (100 μL × 2), and 100 μL of phenol red-free DMEM was added. Fluorescence intensity was quantified immediately using

a BioTek Cytation 5 analyzer. Each of the experiments was conducted in three biological replicates.

Measurement of Intracellular Superoxide and Hydroxyl Radi-cals—HeLa cells were seeded at a density of 0.75×10^6 cells in a six-well plate and allowed to grow overnight. Cells were then treated with 10 μM compound **1** for 4 h. The cells were harvested by trypsinization, washed with ice-cold PBS, and centrifuged at 1200 rpm for 5 min at 4 °C, and the supernatants were discarded. Cells were then incubated with DHE (final conc. 10 μM) or HPF (final conc. 10 μM) in 100 μL of PBS for 30 min at 37 °C in an incubator. Then, 400 μL of PBS was added to the cell suspension and centrifuged, and the supernatant was discarded. The cell pellet was resuspended in 300 μL and analyzed immediately using fluorescence-activated cell sorting (FACS) on a BD FACS ARIA system (488 nm and 561 nm for HPF and DHE dyes, respectively). Approximately 20,000 cells were analyzed. The data were analyzed using FlowJo Software V10.

JC-1 Assay—HeLa cells (0.75 million) were seeded in 35 mm tissue culture plates (2 mL of medium) and allowed to grow for ~24 h. Then, the medium was replaced with fresh medium containing different concentrations of **1** (10 μM, 20 μM, or 40 μM) and incubated for 24 h. Carbonyl cyanide *m*-chlorophenyl hydrazone (CCCP, Sigma) was used as a positive control (50 μM, 5 min incubation). Then, the medium was aspirated, and the cells were washed with PBS (2 × 2 mL), harvested by trypsinization, pelleted, and washed with ice-cold PBS (0.5 mL). The cell pellet was resuspended in 0.5 mL of pre-warmed PBS, and to the tube was added JC-1 dye (2 μM) and incubated for 25 min in the dark at 37 °C in 5% CO_2. Subsequently, the cells were analyzed using a flow cytometer (BD LSRFortessa). The data were analyzed using FlowJo Software V10.

Imaging of 1-Treated ER-RFP and Mito-GFP-Labeled HeLa Cells—HeLa cells were plated (0.5×10^6 cells) in a 35 mm Petri dish and allowed to grow overnight. Following the manufacturer's protocol (Thermo Fisher), the cells were transfected either using CellLight ER-RFP BacMam 2.0 (catalog no. C10591) or CellLight Mitochondria-GFP BacMam 2.0 (catalog no. C1600) to label ER with RFP (ER-RFP cells) or mitochondria with GFP (mito-GFP cells), respectively. These cells were platted on a glass-bottom confocal Petri dish and allowed to grow overnight. The ER-RFP or mito-GFP cells were treated with compound 1 (20 μM or 40 μM) for 8 h or 24 h. **Pt-Fc-2** (40 μM) was used as the positive control for ER-RFP cells. Medium was then removed and washed with PBS (2 × 1 mL), and phenol red-free medium was added, and the images were acquired immediately using a Zeiss LSM 880 confocal microscope. The mito-GFP cells were excited at 488 nm, and emission was recorded at 500−576 nm. The ER-RFP was excited at 543 nm, and emission was recorded at 584−655 nm. The exposure time for the acquisition of fluorescence images was kept constant for the entire experiment. The images were analyzed using ImageJ software.

Analysis of Annexin-V-APC/PI Double-Stained HeLa Cells by Flow Cytometry —HeLa cells were seeded at a density of 0.75×10^6 cells in a 35 mm Petri dish and allowed to grow overnight. Cells were then treated with the compound 1 (10 μM, 20 μM,

or 40 μM, 24 h) or cisplatin (10 μM) or H_2O_2 (10 mM, 15 min) and incubated at 37 °C with 5% CO_2. The cells were harvested by trypsinization, washed with ice-cold PBS, and centrifuged at 1200 rpm for 5 min at 4 °C, and the supernatants were discarded. The cell pellet was resuspended in 500 μL of Annexin-V binding buffer (1× buffer) and collected by centrifugation at 1200 rpm for 5 min at 4 °C. The cells were then resuspended in 350 μL of 1× Annexin-V binding buffer. 5 μL of Annexin-V-APC and 2 μL of propidium iodide (1 mg mL^{-1}) were added, and cells were incubated at 37 °C for 15 min. Then, 150 μL of 1× Annexin-V binding buffer was added and centrifuged at 1200 rpm for 5 min at 4 °C, and the supernatant was discarded. The pellet was suspended in 300 μL of 1× PBS, and cells were acquired immediately using the BD LSRFortessa system. The data were analyzed using FlowJo Software V10.

Acridine Orange Assay—HeLa cells in 35 mm tissue culture Petri dishes were treated with 1 (10 μM, 20 μM, and 40 μM for 24 h) or rapamycin (1 μM, 24 h). The medium was then replaced with FBS-free medium containing 1 μM acridine orange dye and incubated for 25 min in the dark at 37 °C in 5% CO_2. Subsequently, the medium was aspirated and washed with PBS (2 mL × 2), and 2 mL of phenol red-free DMEM (with 4% FBS and 1% antibiotic) was added. Fluorescence imaging was performed using a BioTek Cytation 5 analyzer. The cells were imaged using λ_{ex} 377/λ_{em} 447 (green) and λ_{ex} 531/λ_{em} 640 (red). The exposure time for the acquisition of fluorescence images was kept constant for each series of images at each channel.

Mitochondrial Ca^{2+} Concentration—Rhod-2 AM imaging HeLa cells (0.15×10^6) were seeded on a 35 mm confocal Petri dish. When cells reached an approximate 60−70% confluency, the medium was replaced with fresh medium containing 1 (20 μM) and incubated for 8 h. The cells were then incubated with 0.5 μM Rhod-2 AM (R1254MP) for 30 min at 37 °C. Medium was removed and washed with PBS (2 × 1 mL), phenol red-free medium was added, and the image was acquired using a Zeiss LSM 880 confocal microscope. The Rhod-2 AM dye was excited at 543 nm, and emission was recorded at 555−601 nm. The exposure time for the acquisition of fluorescence images was kept constant for the entire experiment. The images were analyzed using ImageJ software. The cellular fluorescence was quantified using ImageJ software, and the corrected total cell fluorescence (CTCF) was calculated using the following formula.

$$\text{CTCF} = \text{integrated density} - (\text{area of cell} \times \text{mean fluorescence of background reading})$$

Immunoblotting Analysis—Approximately two million cells were seeded in a 60 mm Petri dish. When the confluency reached 80−90%, cells were treated with desired concentrations of test compounds for a required period. Medium was then aspirated, and cells were washed with ice-cold PBS and scrapped into 150 μL of RIPA lysis buffer containing 1× protease inhibitors. The lysate was then centrifuged, and the supernatant was mixed with 4× Laemmli buffer (final concentration 1.25×) and incubated at 90 °C for 10 min. The cell lysates were then resolved by 10 and 12% sodium dodecylsulfate polyacrylamide gel electrophoresis (SDS-PAGE; 120−150 V for 60 min) followed by

electro-transfer to a polyvinylidene difluoride membrane, PVDF (300 mA for 2.5 h). Membranes were blocked using 2% (w/v) skim milk in 0.1% Tween 20 in PBS (TBST) for 30 min, and the solution was decanted, and the membrane was incubated with the primary antibody in a ratio of 1:1000 primary antibodies in TBS overnight at 4 °C. On the following day, after washing with TBST (3 × 2 mL), the membrane was incubated with horseradish peroxidase-conjugated secondary antibodies (Cell Signaling Technology) in TBS in a ratio of 0.75:1000. Immune complexes were detected with the ECL detection reagent (Thermo Fisher) and analyzed using the Bio-Rad ChemiDoc system. List of primary antibodies used from Cell Signaling Technology: Parp antibody (9542L), cleaved caspase-3 (9664L), γ-H2AX (2577L), RIP1 antibody (4926S), RIP3 (95702S), Phospho-eIF2α (3398S), IRE1α (3294S), ATF-6 (65880S), ubiquitin (43124S), LC3B antibody (2775S), GAPDH (2118L), and β-actin (4967L). Secondary antibody: HRP-linked antibody-7074S (Cell Signaling Technology).

Supplementary Material

Refer to Web version on PubMed Central for supplementary material.

Acknowledgments

We thank Prof. Ankona Datta and Shubhangi Das for providing access to the elemental analyzer and collecting the elemental analysis data. We also gratefully acknowledge the financial support under the project no. RTI4003 from the Department of Atomic Energy (DAE) and Tata Institute of Fundamental Research (TIFR), India. Zebrafish work was supported by the DBT/Wellcome Trust India Alliance Intermediate Fellowship (Ref# IA/I/18/2/504016) to C.P.

Abbreviations

DNA	deoxyribonucleic acid
dpf	days post-fertilization
ER	endoplasmic reticulum
FBS	fetal bovine serum
Fc	ferrocene
hpf	hours post-fertilization
MLKL	mixed lineage kinase like
MPTP	mitochondrial permeability transition pore
MEF	murine epithelial fibroblast
PCV	posterior cardinal vein
Pt	platinum
Pt-Fc	platinum−ferrocene bimetallic hybrid
PARP	poly(ADP−ribose) polymerase

Ru	ruthenium
ROS	reactive oxygen species
RF	resistance factor
Ru-Fc	ruthenium−ferrocene bimetallic hybrid
RIP	receptor interacting protein
SAR	structure−activity relationship
SIVP	sub-intestinal venous plexus
UPR	unfolded protein response
WHO	World Health Organization
WT	wild type

References

(1). Johnstone TC, Suntharalingam K, Lippard SJ. The next Rgeneration of platinum drugs: Targeted Pt(II) agents, nanoparticle delivery, and Pt(IV) prodrugs. Chem Rev. 2016; 116: 3436–3486. [PubMed: 26865551]

(2). Kenny RG, Marmion CJ. Toward multi-targeted platinum and ruthenium DrugsA new paradigm in cancer drug treatment regimens? Chem Rev. 2019; 119: 1058–1137. [PubMed: 30640441]

(3). World Health Organization (WHO) model list for essential medicine–s22nd List. 2021. https://www.who.int/publications/i/item/WHO-MHP-HPS-EML-2021.02

(4). Wheate NJ, Walker S, Craig GE, Oun R. The status of plsatinum anticancer drugs in the clinic and in clinical trials. Dalton Trans. 2010; 39: 8113–8127. [PubMed: 20593091]

(5). Konkankit CC, Marker SC, Knopf KM, Wilson JJ. Anticancer activity of complexes of the third row transition metals, rhenium, osmium, and iridium. Dalton Trans. 2018; 47: 9934–9974. [PubMed: 29904760]

(6). King AP, Wilson JJ. Endoplasmic reticulum stress: an arising target for metal-based anticancer agents. Chem Soc Rev. 2020; 49: 8113–8136. [PubMed: 32597908]

(7). Trondl R, Heffeter P, Kowol CR, Jakupec MA, Berger W, Keppler BK. NKP-1339, the first ruthenium-based anticancer drug on the edge to clinical application. Chem Sci. 2014; 5: 2925–2932.

(8). Murray BS, Babak MV, Hartinger CG, Dyson PJ. The development of RAPTA compounds for the treatment of tumors. Coord Chem Rev. 2016; 306: 86–114.

(9). Anthony EJ, Bolitho EM, Bridgewater HE, Carter OWL, Donnelly JM, Imberti C, Lant EC, Lermyte F, Needham RJ, Palau M, Sadler PJ, et al. Metallodrugs are unique: opportunities and challenges of discovery and development. Chem Sci. 2020; 11: 12888–12917. [PubMed: 34123239]

(10). Alessio E, Messori L. NAMI-A and KP1019/1339, two iconic ruthenium anticancer drug candidates face-to-face: A case story in medicinal inorganic chemistry. Molecules. 2019; 24: 1995. [PubMed: 31137659]

(11). Aird RE, Cummings J, Ritchie AA, Muir M, Morris RE, Chen H, Sadler PJ, Jodrell DI. *In vitro* and *in vivo* activity and cross resistance profiles of novel ruthenium (II) organometallic arene complexes in human ovarian cancer. Br J Cancer. 2002; 86: 1652–1657. [PubMed: 12085218]

(12). Seršen S, Kljun J, Kryeziu K, Panchuk R, Alte B, Körner W, Heffeter P, Berger W, Turel I. Structure-related mode-of-action differences of anticancer organoruthenium complexes with β-diketonates. J Med Chem. 2015; 58: 3984–3996. [PubMed: 25856666]

(13). Gadre S, Manikandan M, Duari P, Chhatar S, Sharma A, Khatri S, Kode J, Barkume M, Kasinathan NK, Nagare M, Patkar M, et al. A rationally designed bimetallic platinum (II)-ferrocene antitumor agent induces non-apoptotic cell death and exerts *in vivo* efficacy. Chem–Eur J. 2022; 28 e202201259 [PubMed: 35638709]

(14). Reshetnikov V, Daum S, Janko C, Karawacka W, Tietze R, Alexiou C, Paryzhak S, Dumych T, Bilyy R, Tripal P, Schmid B, et al. ROS-responsive N-alkylaminoferrocenes for cancer-cell-specific targeting of mitochondria. Angew Chem, Int Ed. 2018; 57: 11943–11946.

(15). Zhou J, Kang Y, Chen L, Wang H, Liu J, Zeng S, Yu L. The drug-resistance mechanisms of five platinum-based antitumor agents. Front Pharmacol. 2020; 11: 343. [PubMed: 32265714]

(16). Makrilia N, Lappa T, Xyla V, Nikolaidis I, Syrigos K. The role of angiogenesis in solid tumours: an overview. Eur J Intern Med. 2009; 20: 663–671. [PubMed: 19818284]

(17). Bielenberg DR, Zetter BR. The contribution of angiogenesis to the process of metastasis. Cancer J. 2015; 21: 267–273. [PubMed: 26222078]

(18). Auzias M, Therrien B, Süss-Fink G, Štěpnička P, Ang WH, Dyson PJ. Ferrocenoyl pyridine arene ruthenium complexes with anticancer properties: synthesis, structure, electrochemistry, and cytotoxicity. Inorg Chem. 2008; 47: 578–583. [PubMed: 18085776]

(19). Tauchman J, Süss-Fink G, Štěpnička P, Zava O, Dyson PJ. Arene ruthenium complexes with phosphinoferrocene amino acid conjugates: Synthesis, characterization and cytotoxicity. J Organomet Chem. 2013; 723: 233–238.

(20). Govender P, Riedel T, Dyson PJ, Smith GS. Regulating the anticancer properties of organometallic dendrimers using pyridylferrocene entities: synthesis, cytotoxicity and DNA binding studies. Dalton Trans. 2016; 45: 9529–9539. [PubMed: 27193373]

(21). Mu C, Prosser KE, Harrypersad S, MacNeil GA, Panchmatia R, Thompson JR, Sinha S, Warren JJ, Walsby CJ. Activation by oxidation: ferrocene-functionalized Ru(II)-arene complexes with anticancer, antibacterial, and antioxidant properties. Inorg Chem. 2018; 57: 15247–15261. [PubMed: 30495936]

(22). Paitandi RP, Gupta RK, Singh RS, Sharma G, Koch B, Pandey DS. Interaction of ferrocene appended Ru(II), Rh(III) and Ir(III) dipyrrinato complexes with DNA/protein, molecular docking and antitumor activity. Eur J Med Chem. 2014; 84: 17–29. [PubMed: 25014746]

(23). Liu Z, Sadler PJ. Organoiridium Complexes: Anticancer Agents and Catalysts. Acc Chem Res. 2014; 47: 1174–1185. [PubMed: 24555658]

(24). Massari S, Desantis J, Nannetti G, Sabatini S, Tortorella S, Goracci L, Cecchetti V, Loregian A, Tabarrini O. Efficient and regioselective one-step synthesis of 7-aryl-5-methyl- and 5-aryl-7-methyl-2-amino-[1,2,4]triazolo[1,5-a]pyrimidine derivatives. Org Biomol Chem. 2017; 15: 7944–7955. [PubMed: 28902220]

(25). Caruso F, Rossi M, Benson A, Opazo C, Freedman D, Monti E, Gariboldi MB, Shaulky J, Marchetti F, Pettinari R, Pettinari C. Ruthenium–arene complexes of curcumin: X-ray and density functional theory structure, synthesis, and spectroscopic characterization, in vitro antitumor activity, and DNA docking studies of (p-cymene)Ru(curcuminato)chloro. J Med Chem. 2012; 55: 1072–1081. [PubMed: 22204522]

(26). Fernández R, Melchart M, Habtemariam A, Parsons S, Sadler PJ. Use of chelating ligands to tune the reactive site of half-sandwich ruthenium(II)–arene anticancer complexes. Chem–Eur J. 2004; 10: 5173–5179. [PubMed: 15372674]

(27). Briš A, Jašík J, Turel I, Roithová J. Anti-cancer organoruthenium(ii) complexes and their interactions with cysteine and its analogues. A mass-spectrometric study. Dalton Trans. 2019; 48: 2626–2634. [PubMed: 30702097]

(28). Alberts DS. Carboplatin versus cisplatin in ovarian cancer. Semin Oncol. 1995; 22: 88–90.

(29). Yellol J, Pérez SA, Buceta A, Yellol G, Donaire A, Szumlas P, Bednarski PJ, Makhloufi G, Janiak C, Espinosa A, Ruiz JC. Novel C,N-Cyclometalated Benzimidazole Ruthenium(II) and Iridium(III) Complexes as Antitumor and Antiangiogenic Agents: A Structure-Activity Relationship Study. J Med Chem. 2015; 58: 7310–7327. [PubMed: 26313136]

(30). Paul Gleeson, M, Leeson, PD, Waterbeemd, Hvd. The Handbook of Medicinal Chemistry: Principles and Practice. The Royal Society of Chemistry; 2015. 1–31.

(31). Al-Abd AM, Alamoudi AJ, Abdel-Naim AB, Neamatallah TA, Ashour OM. Anti-angiogenic agents for the treatment of solid tumors: Potential pathways, therapy and current strategies - A review. J Adv Res. 2017; 8: 591–605. [PubMed: 28808589]

(32). Howe K, Clark MD, Torroja CF, Torrance J, Berthelot C, Muffato M, Collins JE, Humphray S, McLaren K, Matthews L, McLaren S, et al. The zebrafish reference genome sequence and its relationship to the human genome. Nature. 2013; 496: 498–503. [PubMed: 23594743]

(33). Gemberling M, Bailey TJ, Hyde DR, Poss KD. The zebrafish as a model for complex tissue regeneration. Trends Genet. 2013; 29: 611–620. [PubMed: 23927865]

(34). Karas BF, Hotz JM, Gural BM, Terez KR, DiBona VL, Côrte-Real L, Valente A, Buckley BT, Cooper KR. Anticancer activity and *in vitro* to *in vivo* mechanistic recapitulation of novel ruthenium-based metallodrugs in the zebrafish model. Toxicol Sci. 2021; 182: 29–43. [PubMed: 33822233]

(35). Jiang J, Cao B, Chen Y, Luo H, Xue J, Xiong X, Zou T. Alkylgold(III) complexes undergo unprecedented photo-induced β-hydride elimination and reduction for targeted cancer therapy. Angew Chem, Int Ed. 2022; 61 e202201103

(36). Hanif M, Arshad J, Astin JW, Rana Z, Zafar A, Movassaghi S, Leung E, Patel K, Söhnel T, Reynisson J, Sarojini V, et al. A multitargeted approach: Organorhodium anticancer agent based on vorinostat as a potent histone deacetylase inhibitor. Angew Chem, Int Ed. 2020; 59: 14609–14614.

(37). Isogai S, Horiguchi M, Weinstein BM. The vascular anatomy of the developing zebrafish: an atlas of embryonic and early larval development. Dev Biol. 2001; 230: 278–301. [PubMed: 11161578]

(38). Goi M, Childs SJ. Patterning mechanisms of the sub-intestinal venous plexus in zebrafish. Dev Biol. 2016; 409: 114–128. [PubMed: 26477558]

(39). Morris RE, Aird RE, del Socorro Murdoch P, Chen H, Cummings J, Hughes ND, Parsons S, Parkin A, Boyd G, Jodrell DI, Sadler PJ. Inhibition of cancer cell growth by ruthenium(II) arene complexes. J Med Chem. 2001; 44: 3616–3621. [PubMed: 11606126]

(40). Scolaro C, Bergamo A, Brescacin L, Delfino R, Cocchietto M, Laurenczy G, Geldbach TJ, Sava G, Dyson PJ. In vitro and in vivo evaluation of ruthenium(II)–arene PTA complexes. J Med Chem. 2005; 48: 4161–4171. [PubMed: 15943488]

(41). Swarts JC, Vosloo TG, Cronje SJ, Du Plessis WC, Van Rensburg CE, Kreft E, Van Lier JE. Cytotoxicity of a series of ferrocene-containing beta-diketones. Anticancer Res. 2008; 28: 2781–2784. [PubMed: 19035310]

(42). Osella D, Ferrali M, Zanello P, Laschi F, Fontani M, Nervi C, Cavigiolio G. On the mechanism of the antitumor activity of ferrocenium derivatives. Inorg Chim Acta. 2000; 306: 42–48.

(43). Tabbí G, Cassino C, Cavigiolio G, Colangelo D, Ghiglia A, Viano I, Osella D. Water stability and cytotoxic activity relationship of a series of ferrocenium derivatives. ESR insights on the radical production during the degradation process. J Med Chem. 2002; 45: 5786–5796. [PubMed: 12477361]

(44). Szatrowski TP, Nathan CF. Production of large amounts of hydrogen peroxide by human tumor cells. Cancer Res. 1991; 51: 794–798. [PubMed: 1846317]

(45). Wu Y, Guo T, Qiu Y, Lin Y, Yao Y, Lian W, Lin L, Song J, Yang H. An inorganic prodrug, tellurium nanowires with enhanced ROS generation and GSH depletion for selective cancer therapy. Chem Sci. 2019; 10: 7068–7075. [PubMed: 31588274]

(46). Wang Y, Yin W, Ke W, Chen W, He C, Ge Z. Multifunctional polymeric micelles with amplified Fenton reaction for tumor ablation. Biomacromolecules. 2018; 19: 1990–1998. [PubMed: 29420880]

(47). Ma, Pa; Xiao, H; Yu, C; Liu, J; Cheng, Z; Song, H; Zhang, X; Li, C; Wang, J; Gu, Z; Lin, J. Enhanced cisplatin chemotherapy by iron oxide nanocarrier-mediated generation of highly toxic reactive oxygen species. Nano Lett. 2017; 17: 928–937. [PubMed: 28139118]

(48). Chow MJ, Licona C, Pastorin G, Mellitzer G, Ang WH, Gaiddon C. Structural tuning of organoruthenium compounds allows oxidative switch to control ER stress pathways and bypass multidrug resistance. Chem Sci. 2016; 7: 4117–4124. [PubMed: 30155055]

(49). du Plessis C, Vosloo G, Swarts CJ. β-Diketones containing a ferrocenyl group: synthesis, structural aspects, pKa1 values, group electronegativities and complexation with rhodium(I). J Chem Soc, Dalton Trans. 1998. 2507–2514.

(50). Kalyanaraman B, Darley-Usmar V, Davies KJ, Dennery PA, Forman HJ, Grisham MB, Mann GE, Moore K, Roberts LJ 2nd, Ischiropoulos H. Measuring reactive oxygen and nitrogen species with fluorescent probes: challenges and limitations. Free Radicals Biol Med. 2012; 52: 1–6.

(51). de Holanda GS, dos Santos Valença S, Carra AM, Lichtenberger RCL, de Castilho B, Franco OB, de Moraes JA, Schanaider A. Translational application of fluorescent molecular probes for the detection of reactive oxygen and nitrogen species associated with intestinal reperfusion injury. Metabolites. 2021; 11: 802. [PubMed: 34940560]

(52). Mohapatra S, Das G, Gupta V, Mondal P, Nitani M, Ie Y, Chatterjee S, Aso Y, Ghosh S. Power of an organic electron acceptor in modulation of intracellular mitochondrial reactive oxygen species: Inducing JNK- and caspase-dependent apoptosis of cancer cells. ACS Omega. 2021; 6: 7815–7828. [PubMed: 33778293]

(53). Sumkhemthong S, Prompetchara E, Chanvorachote P, Chaotham C. Cisplatin-induced hydroxyl radicals mediate pro-survival autophagy in human lung cancer H460 cells. Biol Res. 2021; 54: 22. [PubMed: 34321115]

(54). Lu N, Deng Z, Gao J, Liang C, Xia H, Zhang P. An osmium-peroxo complex for photoactive therapy of hypoxic tumors. Nat Commun. 2022; 13 2245 [PubMed: 35473926]

(55). Pan Z-Y, Tan C-P, Rao L-S, Zhang H, Zheng Y, Hao L, Ji L-N, Mao Z-W. Recoding the cancer epigenome by intervening in metabolism and iron homeostasis with mitochondria-targeted rhenium(I) complexes. Angew Chem, Int. 2020; 59: 18755–18762.

(56). Zhu Z, Wang Z, Zhang C, Wang Y, Zhang H, Gan Z, Guo Z, Wang X. Mitochondrion-targeted platinum complexes suppressing lung cancer through multiple pathways involving energy metabolism. Chem Sci. 2019; 10: 3089–3095. [PubMed: 30996891]

(57). Yoon MJ, Lee AR, Jeong Ah, Kim Y-S, Yeop Kim J, Kwon Y-J, Sook Choi K. Release of Ca2+ from the endoplasmic reticulum and its subsequent influx into mitochondria trigger celastrol-induced paraptosis in cancer cells. Oncotarget. 2014; 5: 6816. [PubMed: 25149175]

(58). Tan C-P, Lu Y-Y, Ji L-N, Mao Z-W. Metallomics insights into the programmed cell death induced by metal-based anticancer compounds. Metallomics. 2014; 6: 978–995. [PubMed: 24668273]

(59). Wlodkowic, D, Skommer, J, Darzynkiewicz, Z. Apoptosis: Methods and Protocols. 2nd ed. Erhardt, P, Toth, A, editors. Humana Press; 2009. 19–32.

(60). Tang D, Kang R, Berghe TV, Vandenabeele P, Kroemer G. The molecular machinery of regulated cell death. Cell Res. 2019; 29: 347–364. [PubMed: 30948788]

(61). Karna P, Zughaier S, Pannu V, Simmons R, Narayan S, Aneja R. Induction of reactive oxygen species-mediated autophagy by a novel microtubule-modulating agent. J Biol Chem. 2010; 285: 18737–18748. [PubMed: 20404319]

(62). SenthilKumar G, Skiba JH, Kimple RJ. High-throughput quantitative detection of basal autophagy and autophagic flux using image cytometry. BioTechniques. 2019; 67: 70–73. [PubMed: 31238709]

(63). Conrad M, Angeli JPF, Vandenabeele P, Stockwell BR. Regulated necrosis: disease relevance and therapeutic opportunities. Nat Rev Drug Discovery. 2016; 15: 348–366. [PubMed: 26775689]

(64). Huang C, Luo Y, Zhao J, Yang F, Zhao H, Fan W, Ge P. Shikonin kills glioma cells through necroptosis mediated by RIP-1. PLoS One. 2013; 8 e66326 [PubMed: 23840441]

(65). Sosna J, Voigt S, Mathieu S, Lange A, Thon L, Davarnia P, Herdegen T, Linkermann A, Rittger A, Chan FK, Kabelitz D, et al. TNF-induced necroptosis and PARP-1-mediated necrosis represent distinct routes to programmed necrotic cell death. Cell Mol Life Sci. 2014; 71: 331–348. [PubMed: 23760205]

(66). Aredia F, Scovassi AI. Poly(ADP-ribose): A signaling molecule in different paradigms of cell death. Biochem Pharmacol. 2014; 92: 157–163. [PubMed: 24976506]

(67). Karch J, Molkentin JD. Regulated necrotic cell death. Circ Res. 2015; 116: 1800–1809. [PubMed: 25999420]

(68). Law BYK, Mok SWF, Chan WK, Xu SW, Wu AG, Yao XJ, Wang JR, Liu L, Wong VKW. Hernandezine, a novel AMPK activator induces autophagic cell death in drug-resistant cancers. Oncotarget. 2016; 7: 8090–8104. [PubMed: 26811496]

(69). Erler JT, Cawthorne CJ, Williams KJ, Koritzinsky M, Wouters BG, Wilson C, Miller C, Demonacos C, Stratford IJ, Dive C. Hypoxia-mediated down-regulation of Bid and Bax in tumors occurs via hypoxia-inducible factor 1-dependent and -independent mechanisms and contributes to drug resistance. Mol Cell Biol. 2004; 24: 2875–2889. [PubMed: 15024076]

(70). Olejniczak SH, Clements JL, Bangia N, Hernandez-Ilizaliturri FJ, Czuczman MS. Down-regulation of Bax and Bak in immuno-chemotherapy resistant non-hodgkin's lymphoma cells. Blood. 2006; 108: 4758.

(71). Teleanu RI, Chircov C, Grumezescu AM, Teleanu DM. Tumor angiogenesis and anti-angiogenic strategies for cancer treatment. J Clin Med. 2020; 9: 84.

(72). Sheldrick GM. SHELXT-Integrated space-group and crystal-structure determination. Acta Crystallogr, Sect A: Found Adv. 2015; 71: 3–8. [PubMed: 25537383]

(73). Sheldrick GM. Crystal structure refinement withSHELXL. Acta Crystallogr, Sect C: Struct Chem. 2015; 71: 3–8. [PubMed: 25567568]

(74). Dolomanov OV, Bourhis LJ, Gildea RJ, Howard JAK, Puschmann H. OLEX2: a complete structure solution, refinement and analysis program. J Appl Crystallogr. 2009; 42: 339–341.

(75). Proulx K, Lu A, Sumanas S. Cranial vasculature in zebrafish forms by angioblast cluster-derived angiogenesis. Dev Biol. 2010; 348: 34–46. [PubMed: 20832394]

(76). Kimmel CB, Ballard WW, Kimmel SR, Ullmann B, Schilling TF. Stages of embryonic development of the zebrafish. Dev Dyn. 1995; 203: 253–310. [PubMed: 8589427]

Europe PMC Funders Author Manuscripts

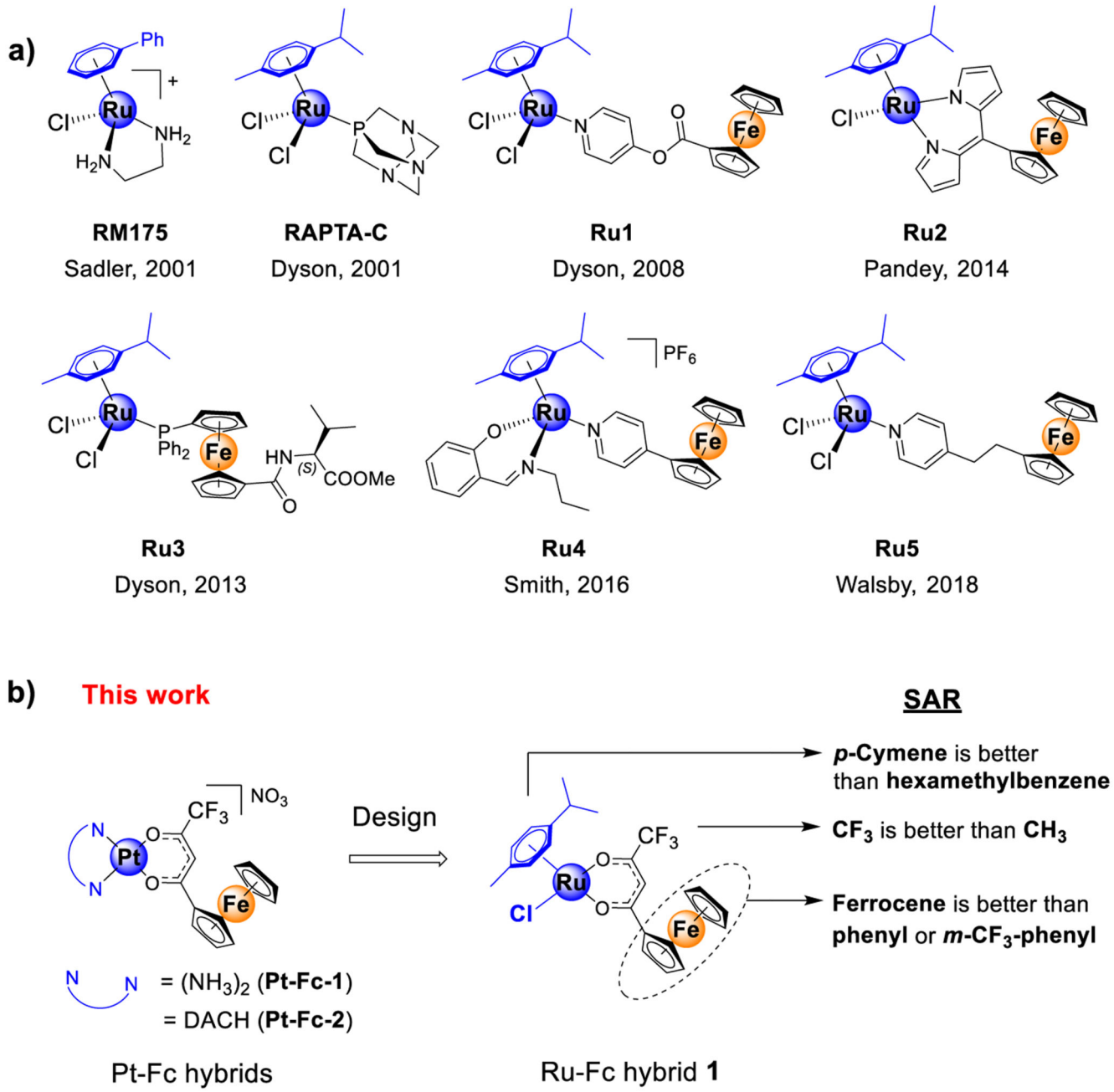

Figure 1.

(a) Structures of previously reported archetypical Ru(η^6-arene) complexes (RM175 and RAPTA-C) and selected examples of Ru(η^6-arene)-Fc (Fc = ferrocene) bimetallic derivatives (**Ru1**−**Ru5**) with anticancer properties. (b) Schematic presentation of the design of Ru(η^6-arene)-Fc compound **1** employed in this study. The [Pt(N−N)] moiety in Pt-Fc (**Pt-Fc-1** and **-2**) bimetallic anticancer compounds was replaced with a [Ru(η^6-arene)Cl] moiety. DACH = 1*R*,2*R*-diaminocyclohexane.

Europe PMC Funders Author Manuscripts

Europe PMC Funders Author Manuscripts

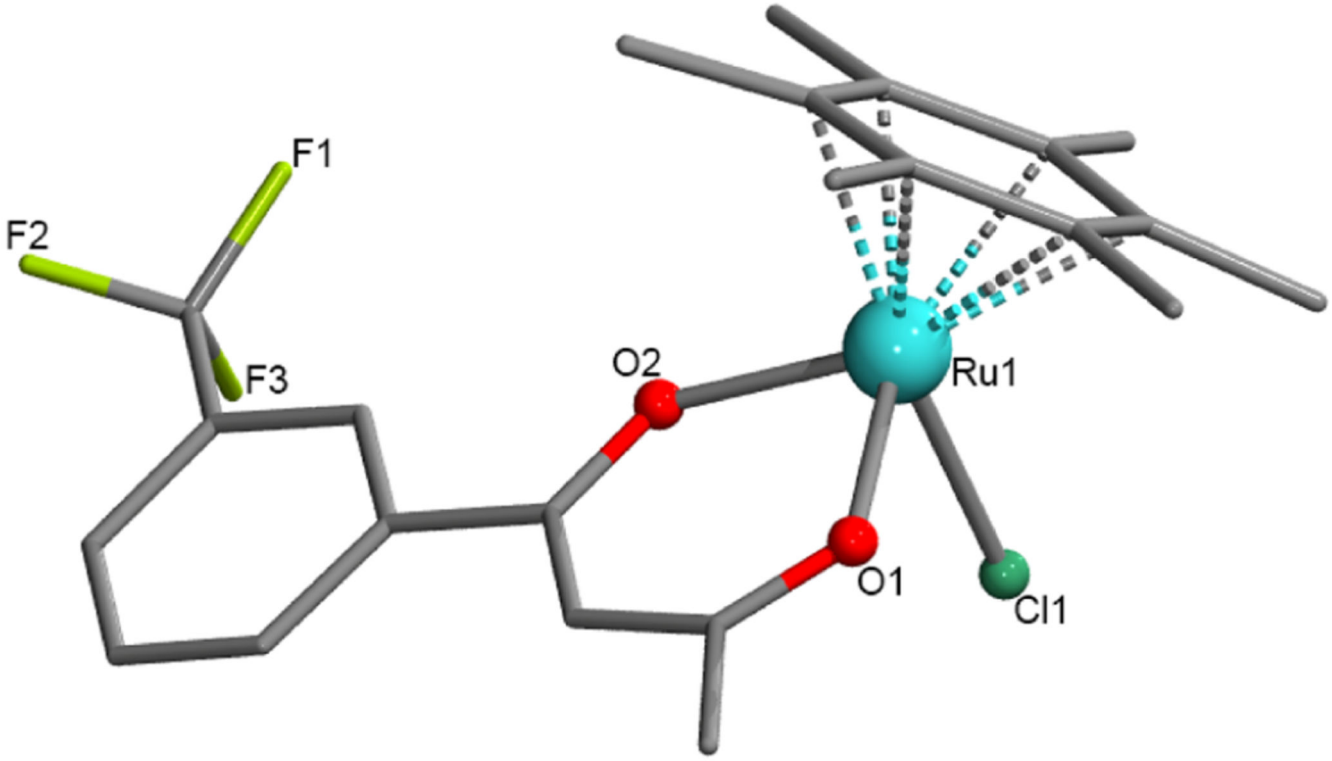

Figure 2.

Crystal structure of [Ru(η^6-C_6Me_6)(CF_3-Ar^{-acac})Cl] (6). Hydrogen atoms are omitted for clarity, and the dotted Ru−C bonds show Ru-(η^6-arene) binding of C_6Me_6. CCDC deposition number 2190222 that contains the supplementary crystallographic data for this paper.

Europe PMC Funders Author Manuscripts

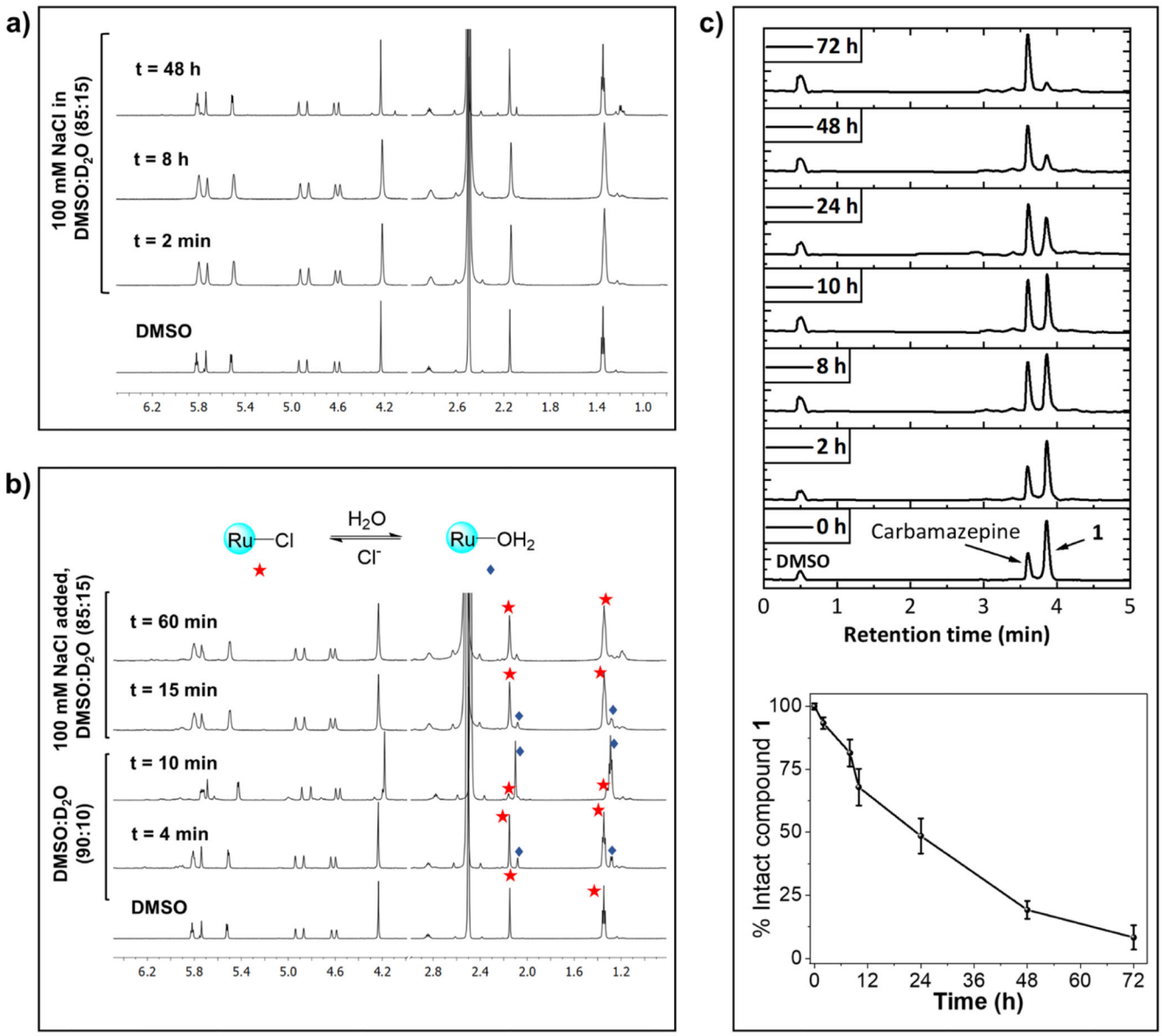

Figure 3.

(a) Stability of **1** in DMSO-d_6/D_2O containing 100 mM NaCl. (b) Reversible aquation and anation of **1**. ^1H NMR spectra of 1 in DMSO-d_6/D_2O are measured till aquation is completed. Then, concentrated NaCl solution in D_2O was added, and ^1H NMR was recorded at different time points. (c) Top: stacked UPLC chromatograms of a mixture of **1** and carbamazepine (internal standard) in RPMI (with 10% FBS) at different time points. Bottom: percent of intact **1** remaining in RPMI at different time points calculated from the ratio of **1** and carbamazepine.

Europe PMC Funders Author Manuscripts

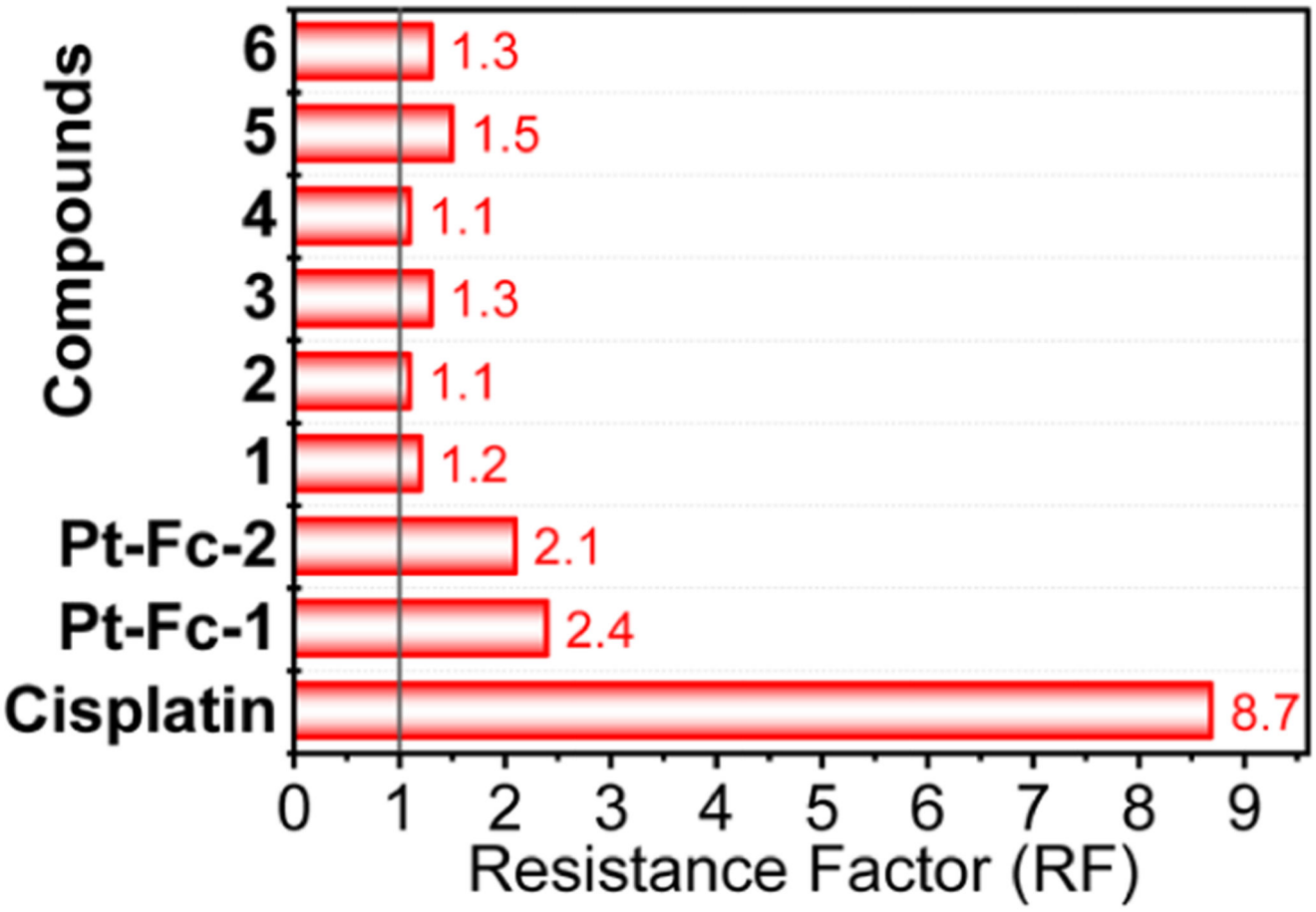

Figure 4. Comparison of the RF of 1−6, Pt-Fc-1, Pt-Fc-2, and cisplatin. RF ≤ 1 implies no resistance.

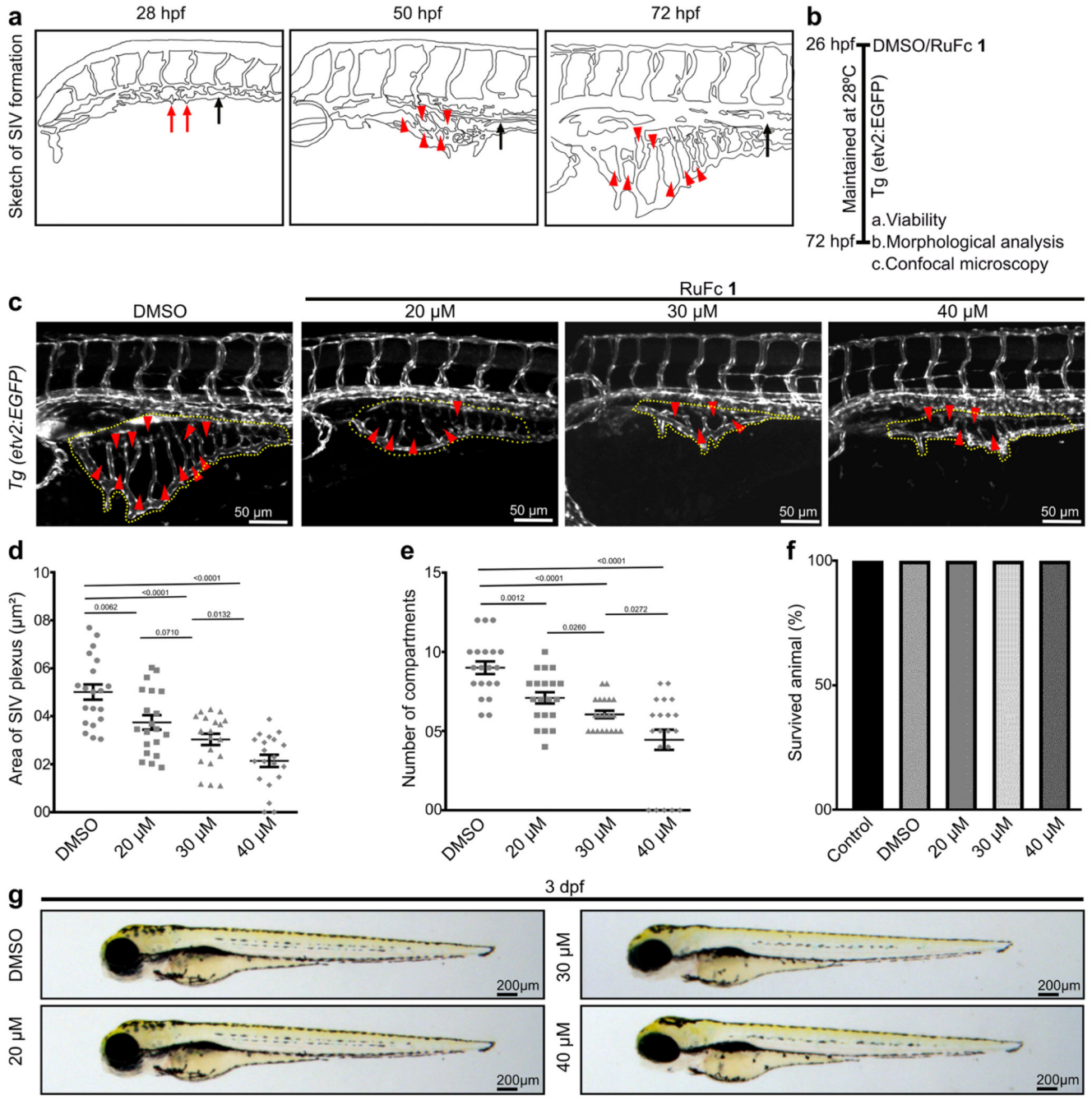

Figure 5. Small-molecule Ru-Fc hybrid 1 is non-toxic and inhibits angiogenesis in zebrafish embryos in a dose-dependent manner.

(a) Schematic representation of SIVP formation in a wild-type embryo. Red arrows indicate angiogenic sprouts from the PCV (black arrow) around 28 hpf (hours post-fertilization). Red arrowheads indicate vascular compartments in SIVPs, and black arrows indicate the PCV at 55 and 72 hpf. (b) Schematic depiction of the experimental procedures. (c) Maximum intensity projections of confocal optical sections of the SIVP of 72 hpf *Tg(etv2:EGFP)* embryos, which express EGFP in the blood vessel endothelial cells. The SIVP area is encircled with a dotted line, and arrowheads denote compartments in the SIVP. (d) Dot

plot depicting the area covered by the SIVP (n = 20). (e) Quantification of the number of compartments in SIVPs (n = 20). (f) Histogram depicting the animal viability at 72 hpf (n = 4, 10 embryos in each experiment). (g) Bright-field images of the representative embryos at 3 dpf (days post-fertilization). See Figure S21 for the extended image.

Europe PMC Funders Author Manuscripts

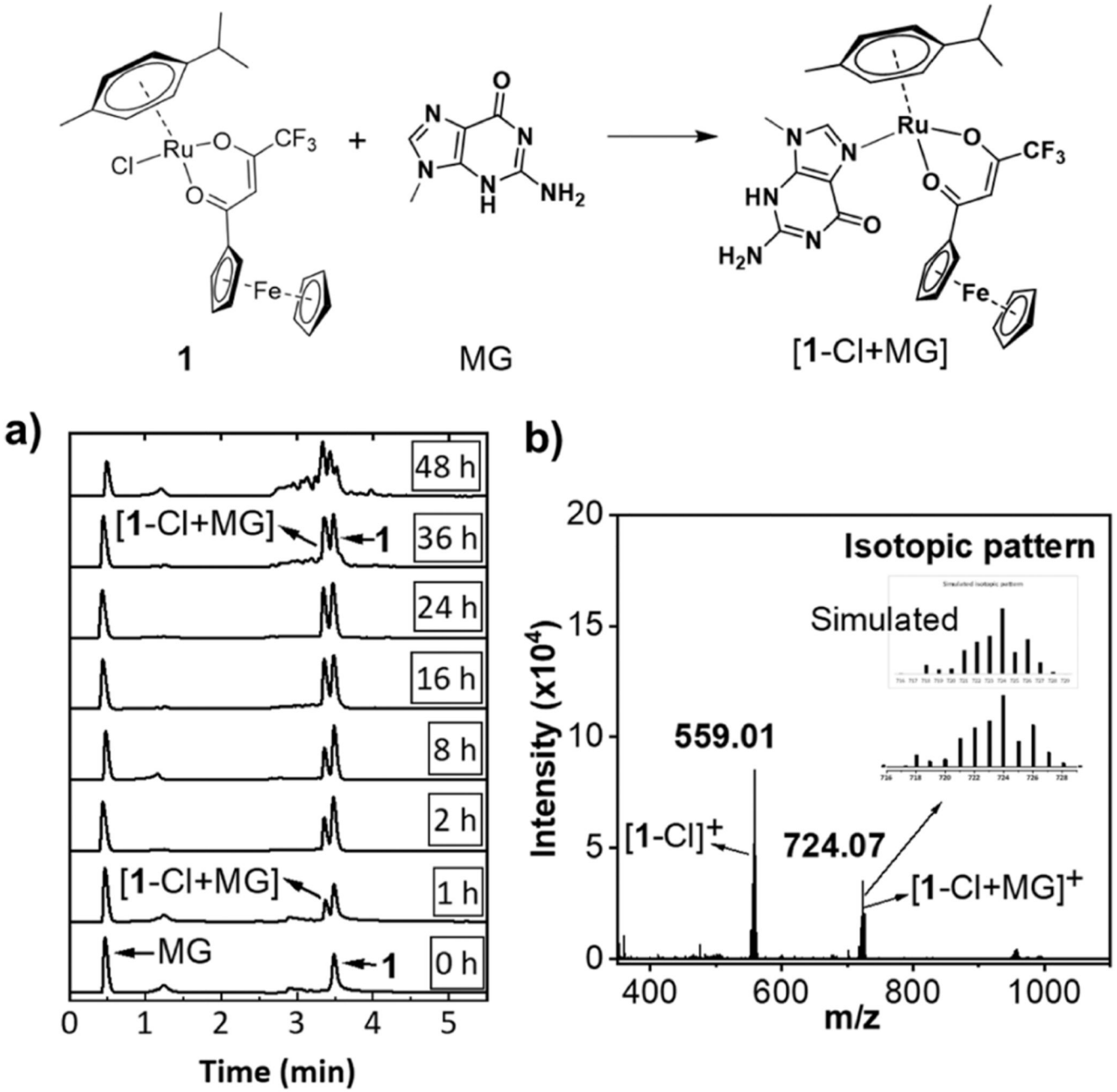

Figure 6. Reactivity of 1 with 9-methylguanine (MG).

(a) Time-dependent UPLC traces (254 nm) of a 1:1 mixture of **1** and MG incubated at 37 °C.

(b) ESI mass spectrum of a 1:1 mixture of **1** and MG incubated at 37 °C for 36 h.

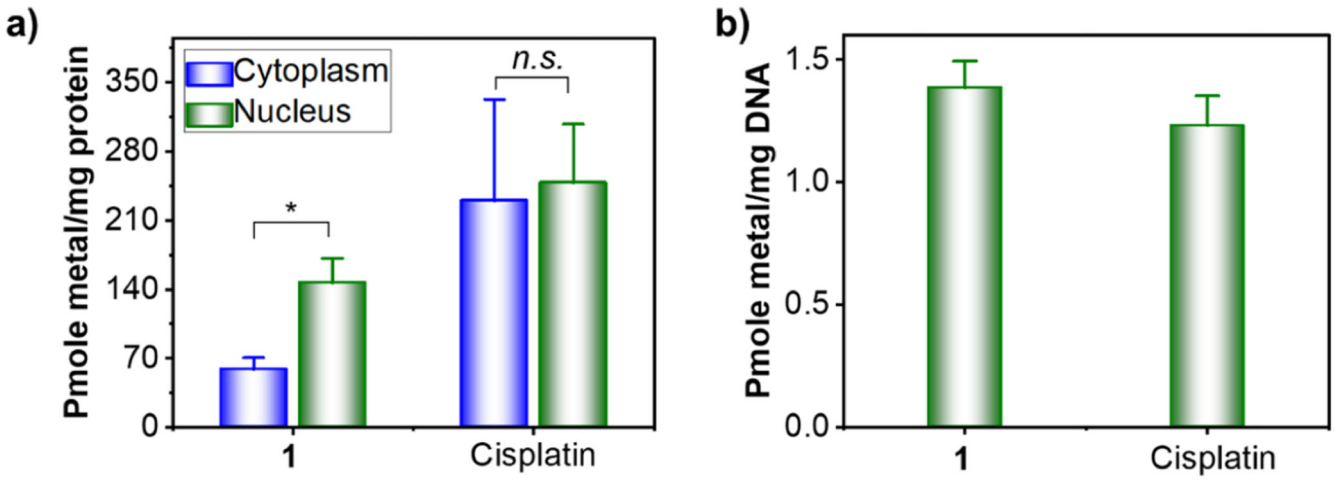

Figure 7.

(a) Intracellular distribution of compound **1** and cisplatin between the nucleus and cytoplasm in Hela cells (10 μM, 24 h exposure). (b) Metalation of genomic DNA of HeLa cells by compound **1** and cisplatin (20 μM, 24 h exposure). Data represents the mean ± SD of three or more replicates (*$p < 0.05$).

Europe PMC Funders Author Manuscripts

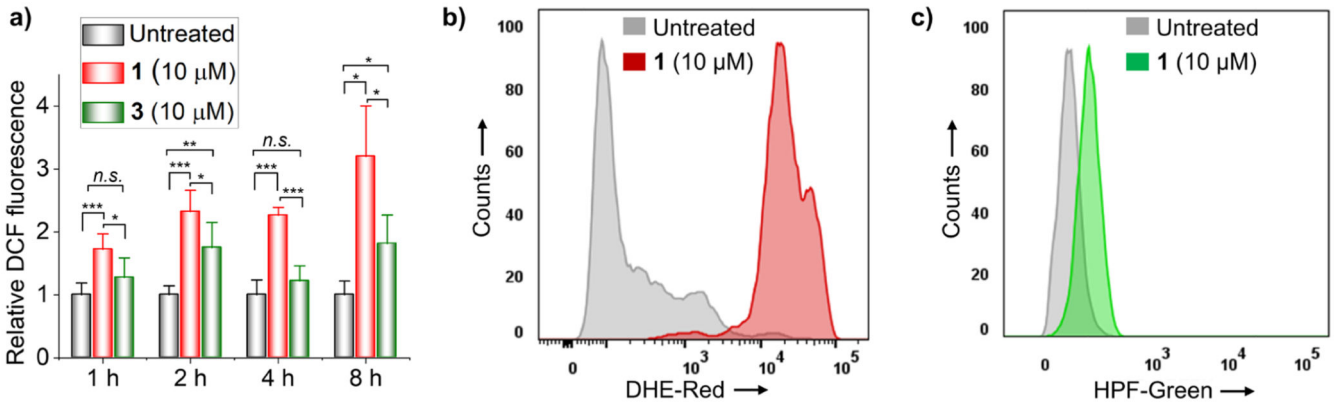

Figure 8.

(a) H_2DCF-DA assay for monitoring the ROS level in HeLa cells treated with **1** or **3** for 1, 2, 4, and 8 h. (b) Flow cytometric quantification of $O_2^{\bullet -}$ radicals in untreated and **1**-treated HeLa cells using the DHE probe (4 h exposure). (c) Flow cytometric quantification of $HO^{\bullet}$ radicals in untreated and **1**-treated HeLa cells using the HPF probe (4 h exposure).

Europe PMC Funders Author Manuscripts

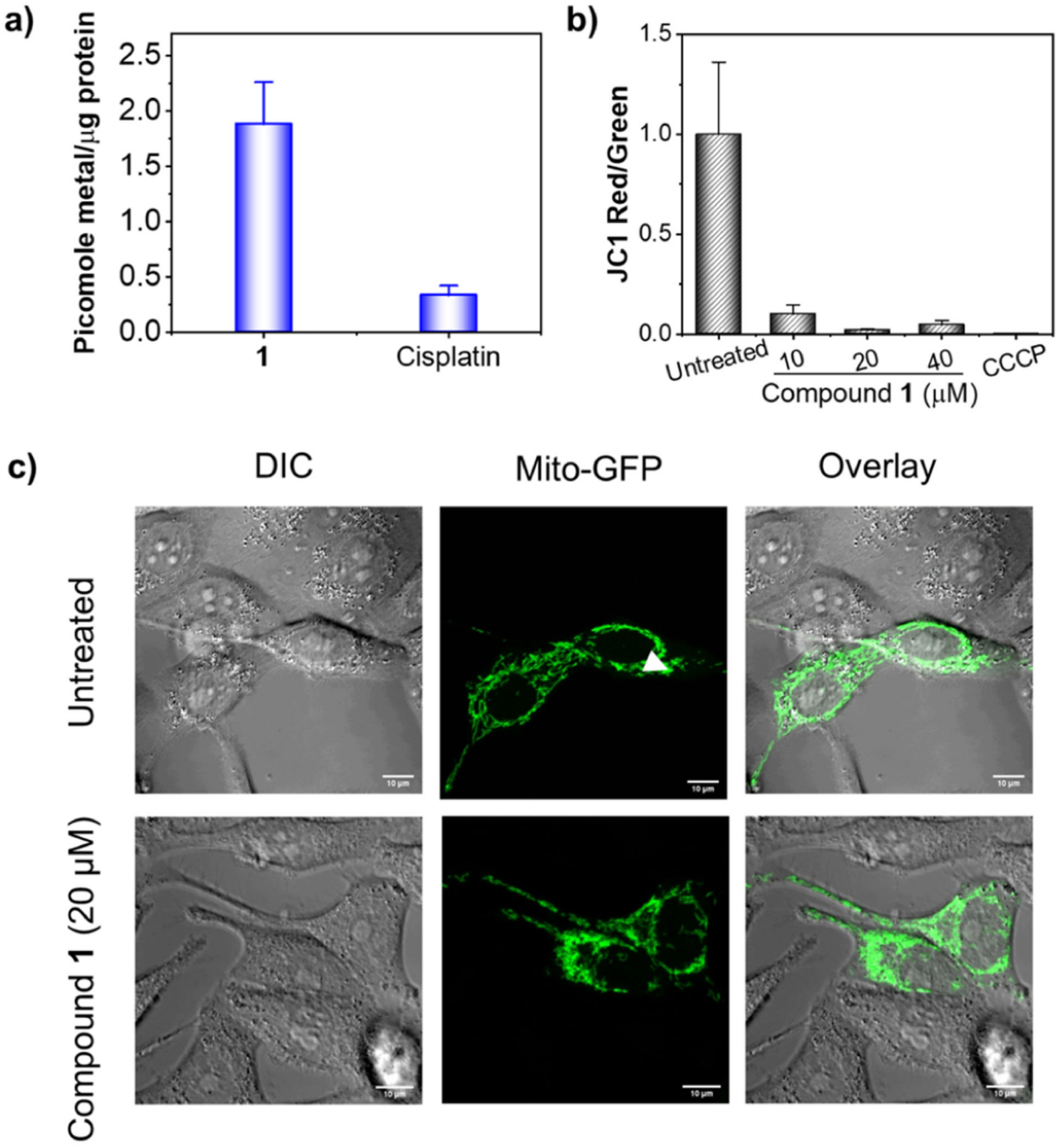

Figure 9.

(a) Quantification of metals in isolated mitochondria of HeLa cells treated with **1** or cisplatin (20 μM, 24 h). (b) Effect of **1** on **ΔΨ**m (as a ratio of JC-1 red/green) from flow cytometric analysis (exposure 24 h). CCCP was used as a positive control (50 μM, 5 min incubation). (c) Comparison of the mitochondrial morphology of untreated and 1-treated HeLa cells with that of the mitochondria labeled with GFP (20 μM, exposure 24 h). Note: concentrations of **1** for the JC-1 assays (b) and mitochondrial morphology analysis (c) were chosen to be 1/4 ×

$IC_{50/24h}$ (10 μM) or 1/2 × $IC_{50/24h}$ (20 μM) or $IC_{50/24h}$ (40 μM) based on the $IC_{50/24h}$ value (38 ± 3 μM) obtained using a 24 h MTT assay.

Europe PMC Funders Author Manuscripts

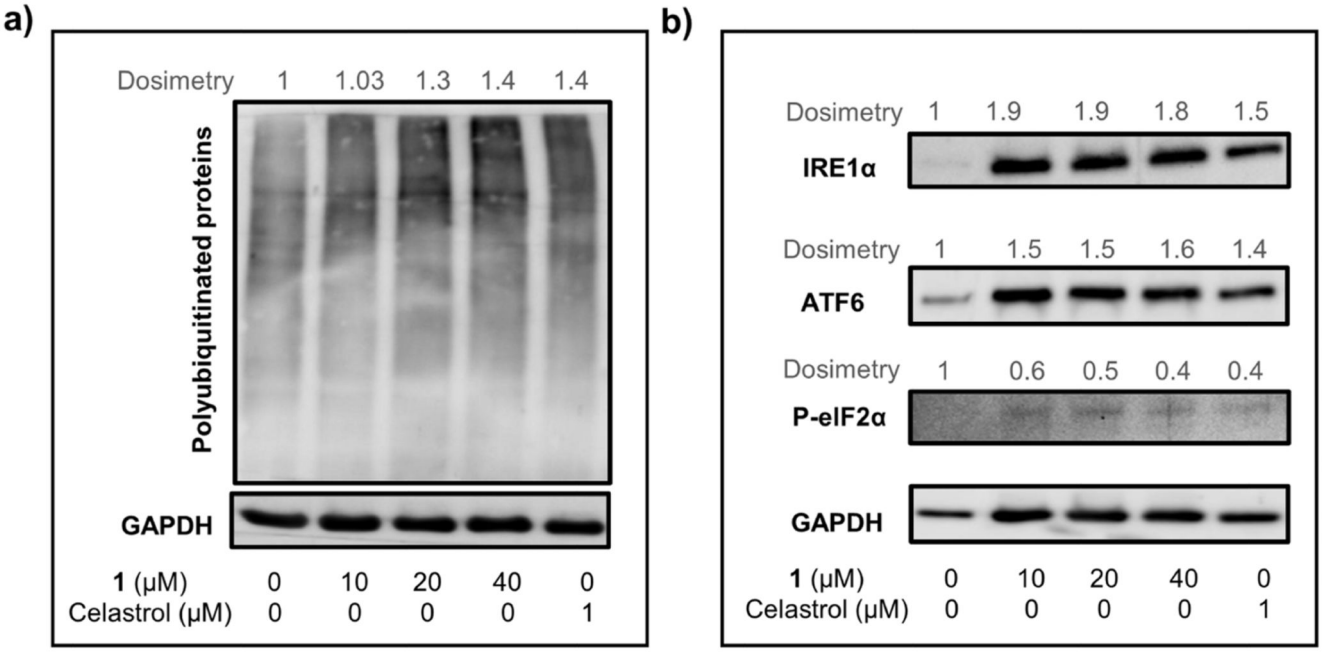

Figure 10.

Western blot analysis of polyubiquitinated proteins (a) and ER-stress marker proteins (b) in HeLa cells treated with increasing concentrations of **1** (1/4 × $IC_{50/24h}$, 1/2 × $IC_{50/24h}$, and $IC_{50/24h}$) or celastrol (positive control) for 24 h.

Europe PMC Funders Author Manuscripts

Europe PMC Funders Author Manuscripts

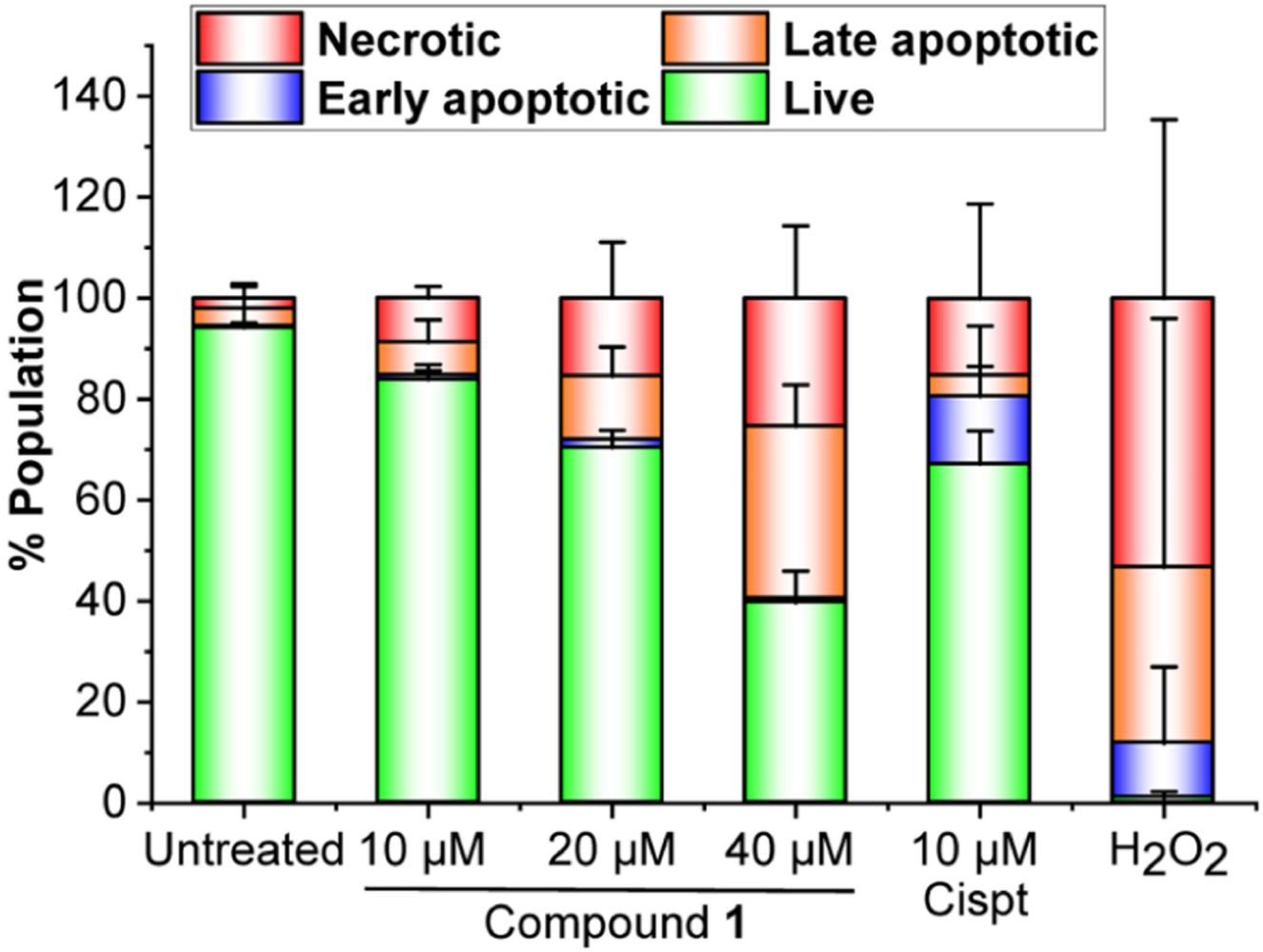

Figure 11.

(a) Flow cytometry analysis of the apoptotic and necrotic population in HeLa cells treated with increasing doses of compound **1** (1/4 × $IC_{50/24h}$, 1/2 × $IC_{50/24h}$, and $IC_{50/24h}$, 24 h exposure), cisplatin (Cispt, 0.7 × $IC_{50/24h}$, 24 h exposure), or H_2O_2 (10 mM, 15 min exposure).

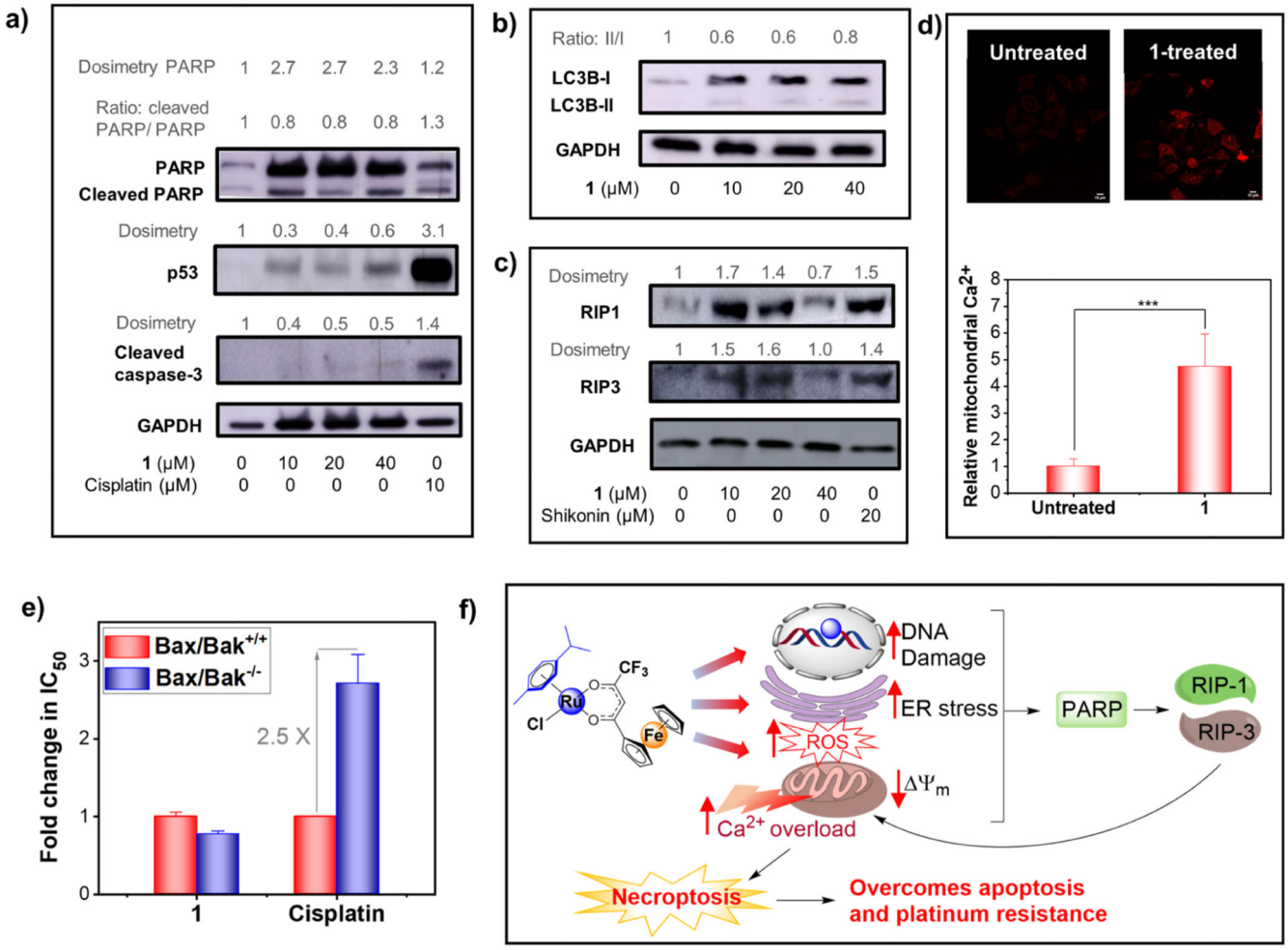

Figure 12.

(a) Western blot analysis of apoptosis-related marker proteins in HeLa cells treated with 1/4 × $IC_{50/24h}$ (10 μM), 1/2 × $IC_{50/24h}$ (20 μM), and $IC_{50/24h}$ (40 μM) concentrations of **1** (24 h compound exposure). (b) Western blot analysis of autophagy marker proteins in HeLa cells treated with concentrations of **1** (24 h compound exposure). (c) Western blot analysis of necroptosis marker proteins in HeLa cells treated with concentrations of **1** (24 h compound exposure). (d) Comparison of the mitochondrial Ca^{2+} level in untreated or 1-treated (20 μM, 24 h) HeLa cells. (e) Fold change in IC_{50} of **1** and cisplatin in the wild-type murine embryonic fibroblast (MEF-Bax/$Bak^{+/+}$) as compared to that in the Bax/Bak double knocked-out (MEF-Bax/$Bak^{-/-}$) cell lines. (f) Proposed cellular mechanism of action of **1**. * denotes statistical significance ($p < 0.05$).

Europe PMC Funders Author Manuscripts

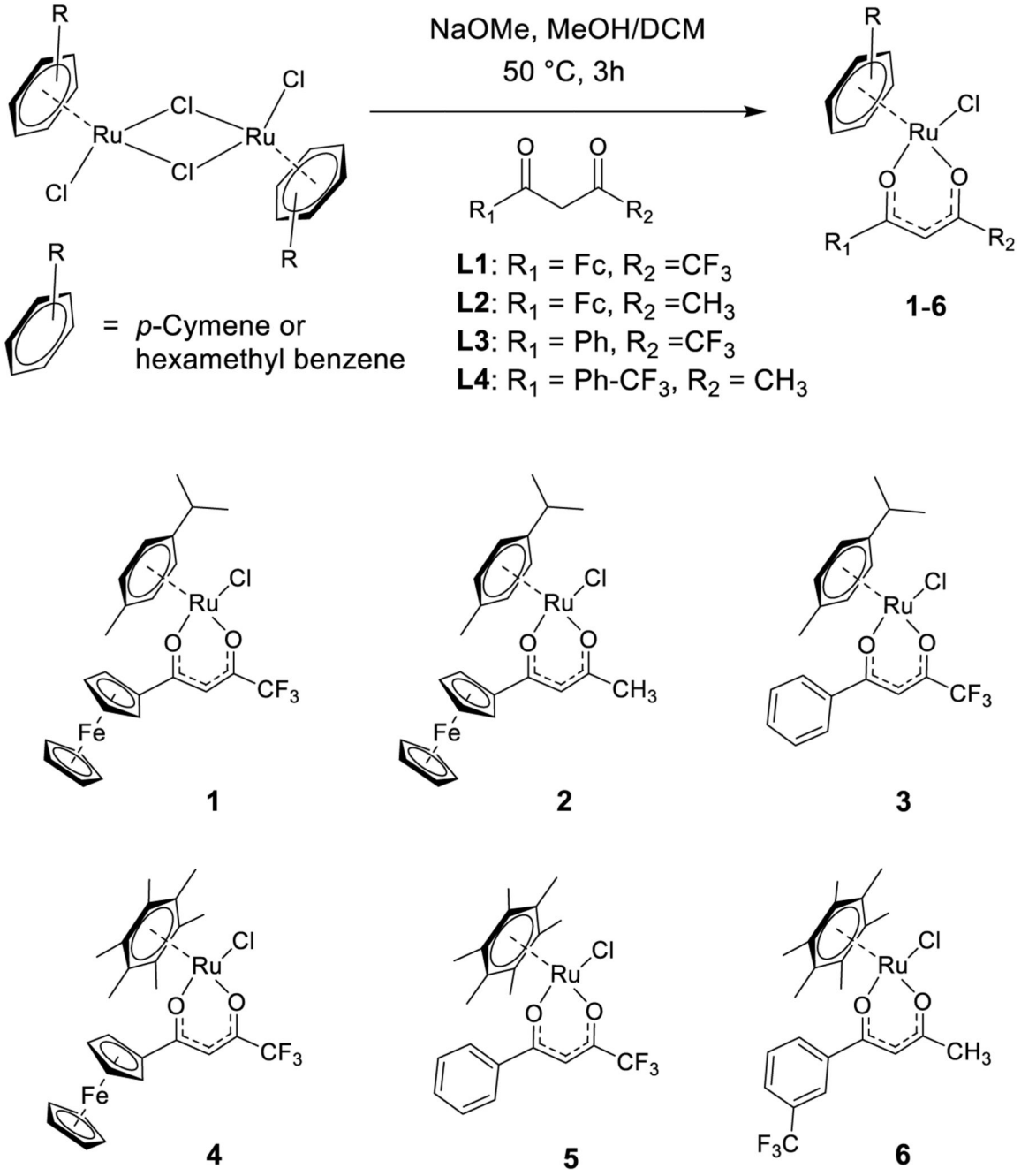

Scheme 1. Synthesis of Ru(II)−Arene-Based Bimetallic (1, 2, and 4) and Monometallic (3, 5, and 6) Complexes

Europe PMC Funders Author Manuscripts

Table 1

Comparison of IC_{50} Values (μM) of **1**−6, L1, Pt-Fc-1, Pt-Fc-2, Ru1, Ru3, Ru4, Cisplatin, and Oxaliplatin (72 h Continuous Exposure, MTT Assay)[a]

compound	HeLa	A2780	A2780cis	RF (A2780)
1	1.3 ± 0.3	2.5 ± 0.3	3.1 ± 0.1	1.2
2	12.7 ± 0.6	48.2 ± 2	51.1 ± 2	1.1
3	30.2 ± 10	20.7 ± 6	26.3 ± 3	1.3
4	8.2 ± 0.6	4.3 ± 0.1	4.6 ± 0.6	1.1
5	13.8 ± 0.6	10.5 ± 2	15.9 ± 0.1	1.5
6	6.1 ± 1	5.1 ± 0.1	6.7 ± 2	1.3
L1	23 ± 0.0[a]	11.4 ± 2[a]		
Pt-Fc-1	4.9 ± 2[a]	2.2 ± 0.1	5.3 ± 1	2.4
Pt-Fc-2	2.8 ± 0.3[a]	1.3 ± 0.1	2.8 ± 0.2	2.1
Ru1		44.4 ± 5[b]	43.4 ± 3[b]	0.9
Ru3		7.8 ± 0.1[c]	14.5 ± 0.0[c]	1.8
Ru4		29.2 ± 2[d]	33.0 ± 2[d]	1.1
cisplatin	3.0 ± 0.1	0.8 ± 0.1	6.7 ± 0.1	8.7
oxaliplatin	2.1 ± 0.3			

[a]Values presented as mean ± standard deviations obtained from three independent experiments each performed in triplicate. Note: *a* = values taken from ref 13, *b* = values taken from ref 18, *c* = values taken from ref 19, *d* = values taken from ref 20, RF = IC_{50} in A2780Cis/IC_{50} in A2780.

Europe PMC Funders Author Manuscripts

Table 2

Lipophilicity (log *P*) and Whole Cell Uptake of 1−6 in HeLa Cells (10 μM, 4 h Exposure)[a]

compound	log *P*	picomole Ru/10^6 cells
1	1.1 ± 0.1	57.0 ± 9.7
2	0.9 ± 0.0	47.8 ± 1.2
3	1.0 ± 0.1	16.5 ± 3.2
4	1.2 ± 0.1	89.5 ± 5.3
5	1.1 ± 0.1	36.4 ± 4.8
6	1.2 ± 0.0	44.2 ± 2.6

[a]Results are presented as mean ± SD from three independent experiments each performed in triplicate.